Draft version July 7, 2014
Preprint typeset using LaTeX style emulateapj v. 12/16/11

HERSCHEL SPECTROSCOPIC OBSERVATIONS OF LITTLE THINGS DWARF GALAXIES

PHIL CIGAN[1], CO-AUTHORS[234](ORDER TBD), AND THE LITTLE THINGS TEAM

Draft version July 7, 2014

ABSTRACT

We present far-infrared spectral line observations of five galaxies from the LITTLE THINGS sample: DDO 69, DDO 70, DDO 75, DDO 155, and WLM. While most studies of dwarfs focus on bright systems or starbursts due to observational constraints, our data extend the observed parameter space into the regime of *normal* dwarf galaxies with low surface brightness, low metallicities, and moderate star formation rates. Our targets were observed with *Herschel* at the [C II] 158μm, [O I] 63μm, [O III] 88μm, and [N II] 122μm emission lines using the PACS Spectrometer. These high-resolution maps allow us for the first time to study the far-infrared properties of these systems on the scales of larger star-forming complexes. Our systems have very bright and widespread [C II] emission, averaging near 0.5% of the total infrared budget - much higher than most other galaxies of any type. [N II] is poorly detected, and even then only after integrating over disparate faint regions, suggesting that the [C II] emission in our galaxies comes mostly from PDRs instead of the diffuse ionized ISM. These systems exhibit efficient cooling at low dust temperatures, as shown by ([O I]+[C II])/TIR, and low [O I]/[C II] ratios indicate that [C II] is the dominant coolant of the ISM.

Subject headings: galaxies: dwarf — galaxies: ISM — galaxies: individual (DDO 69, DDO 70, DDO 75, DDO 155, WLM)

1. INTRODUCTION

Dwarf galaxies present interesting challenges for the studies of various galaxy properties, due in part to their low surface brightness and their typically low metallicity. Generally, we see that stars form out of molecular clouds, whose cores are traced by CO. However, molecular cloud structure is believed to change with metallicity: the lower the abundance of heavier elements, the smaller the pure molecular core becomes while the photodissociation region (PDR) covers a larger fraction (Madden, et al. 1997; Hunter, et al. 2001; Bolatto, et al. 1999; Leroy, et al. 2007; Maloney & Black 1988; Röllig, et al. 2006). This is why CO is hard to detect in dwarfs. Yet, despite the paucity of CO observed in these systems, they could still harbor abundant reservoirs of molecular gas(Leroy, et al. 2008; Hunt, et al. 2010; Leroy, et al. 2007; Bot, et al. 2007; Bolatto, et al. 2008; Leroy, et al. 2009).

To determine the structure of star-forming molecular clouds at low metallicity, we have mapped far-infrared (FIR) fine-structure lines with the *Herschel Space Telescope* in regions of five dwarfs that ~~are~~ part of the LITTLE THINGS (Local Irregulars That Trace Luminosity Extremes, The HI Nearby Galaxy Survey; Hunter, et al. 2012) sample of nearby dwarf galaxies – some of the lowest-metallicity galaxies that have ever been observed at these wavelengths. These specific targets were chosen as a representative sample of *normal* dwarfs – those with only moderate star formation rates and extremely low metallicities ($\sim$ 13% down to $\sim$ 5% $Z_\odot$, where $Z_\odot$ defined by $12 + \log(N_O/N_H)$ is 8.69, Asplund, M., et al. 2009). Basic information about each galaxy in this sample is presented in Table 1.

A single star-forming complex was chosen as the target of observation in each galaxy. The specific regions observed were selected as being most likely to have molecular gas, based on areas of enhanced far-ultraviolet (FUV) and Hα – indicating recent star formation – as well as neutral hydrogen (H I) emission. Figures 1 and 11 (online) show the target regions in comparison to the H I distribution.

We supplement the *Herschel* data with mid- and far-infrared continuum images from the *Spitzer Space Telescope* at 24, 70, and 160 μm, as well as our PACS Photometer 100μm and 160μm maps, where available. We utilize *Infrared Astronomical Satellite* (*IRAS*) 60 and 100 μm measurements, where available, for comparison with previous studies. We also have optical images in V- and B-band (Hunter & Elmegreen 2006), Hα (Hunter & Elmegreen 2004), and FUV (Dale, et al. 2009 for DDO 155; Hunter, et al. 2006 for the rest), for comparison with features and luminosities seen in the infrared, as well as for determining locations and quantifying star formation in our galaxies.

The ratios of several FIR lines tell us ~~a great deal~~ about the physics in these systems. Now, with the enhanced spatial resolution of the PACS spectrometer, we can build on ~~the~~ previous studies that were limited to average fluxes over entire galaxies, and pursue detailed studies in separate resolved regions within each image. We present three different viewpoints on our galaxies: we investigate large regions covering the majority of the real flux observed for bulk comparisons, we target individual resolved regions within each image, and we finally analyze our maps on a pixel-by-pixel basis.

This paper is organized as follows. In § 2 we describe

[1] Physics Department, New Mexico Institute of Mining and Technology, Socorro, NM 87801, USA; pcigan@nmt.edu
[2] Institut für Theoretische Astrophysik, Zentrum für Astronomie der Universität Heidelberg, Albert-Ueberle Str. 2, D-69120 Heidelberg, Germany
[3] Laboratoire AIM, CEA/DSM - CNRS - Université Paris Diderot, Irfu/Service d'Astrophysique, CEA Saclay, 91191 Gif-sur-Yvette, France
[4] Lowell Observatory, 1400 West Mars Hill Road, Flagstaff, AZ 86001, USA

(A) The fine-structure lines allow us to map the PDRs. The dwarf sample is

TABLE 1
BASIC GALAXY INFORMATION

Galaxy	Other Names	D (Mpc)	M_V (mag)	R_H (arcmin)	R_D (kpc)	$E(B-V)_f$	$\log_{10}$ SFR_D^{FUV} ($M_\odot$ yr^{-1} kpc^{-2})	12+$\log_{10}$(O/H)
DDO 69	PGC 28868 UGC 5364 Leo A	0.8	-11.7	2.4	0.19 ± 0.01	0.00	-2.22 ± 0.01	7.4 ± 0.10
DDO 70	PGC 28913 UGC 5373 Sextans B	1.3	-14.1	3.71	0.48 ± 0.01	0.01	-2.16 ± 0.00	7.5 ± 0.06
DDO 75	PGC 29653 UGCA 205 Sextans A	1.3	-13.9	3.09	0.22 ± 0.01	0.02	-1.07 ± 0.01	7.5 ± 0.06
DDO 155	PGC 44491 UGC 8091 GR 8 VII Zw 222	2.2	-12.5	0.95	0.15 ± 0.01	0.01	···	7.7 ± 0.06
WLM	PGC 143 UGCA 444 DDO 221	1.0	-14.4	5.81	0.57 ± 0.03	0.02	-2.05 ± 0.01	7.8 ± 0.06

REFERENCES. — Distances and Metallicities, respectively. DDO 69: Dolphin, et al. (2002), van Zee, et al. (2006). DDO 70: Sakai, et al. (2004), Kniazev, et al. (2005). DDO 75: Dolphin, et al. (2003), Kniazev, et al. (2005). DDO 155: Tolstoy, et al. (1995a), van Zee, et al. (2006). WLM: Gieren, et al. (2008), Lee, et al. (2005).

NOTE. — General information about this galaxy sample, as reported by Hunter, et al. (2012). $E(B\text{-}V)_f$ is the foreground reddening from Burstein & Heiles (1984). R_H is the Holmberg radius, and R_D is the disk scale length. SFR_D^{FUV} is the star formation rate determined from L_{FUV} and divided by πR_D^2.

our collected data and their uncertainty characterization, in § 3 we analyze the FIR flux ratios as well as qualitative features in the maps, and in § 4 we discuss our results in further detail before summarizing in § 5.

1.1. *Origins of FIR Line Emission*

The [C II] 158μm line is one of the primary FIR coolants of the ISM, typically accounting for about 1% of the total FIR energy budget (Stacey, et al. 1991, for example). Existing in radiation fields with photon energies between 11.26-24.38 eV, [C II] can be found in diffuse ionized regions as well as denser regions with molecular gas. Specifically, [C II] can exist at the surface of molecular clouds, which can also harbor dust- or self-shielded H_2 (Tielens & Hollenbach 1985, Wolfire, et al. 2010). We explore the relation between carbon and hydrogen species in our galaxies in an upcoming paper. See Hollenback & Tielens (1997) for their classic review of PDR structure and atomic/molecular species arrangement therein. Also see, e.g., Wolfire, et al. (1990), Bolatto, et al. (1999), and Kaufman, et al. (1999) for additional discussion of the models of FIR line tracers of PDRs.

[O I] emission at 63μm originates in the warm and cold neutral media. Neutral oxygen's ionization potential of 13.62 eV is quite close to that of hydrogen, making it a good tracer of the boundaries of neutral regions. This is one of the main coolants of warm, dense gas, and can exist deeper into PDRs than [C II] because it has a higher hydrogen critical density.

The [O III] 88μm line comes from highly ionized environments. This species requires ionizing radiation of >35.12 eV, which is provided by early O stars in H II regions.

[N II] 122μm emission comes from diffuse, ionized regions, where the radiation is stronger than its ionization potential of 14.53 eV. Since some of the [C II] observed can come from this phase, [N II] can be used to separate the diffuse [C II] component from the PDR emission (Heiles 1994).

2. DATA

2.1. *Observations*

We used the PACS spectrometer (Poglitsch, et al. 2010) aboard *Herschel* (Pilbratt, et al. 2010) to observe the [C II] 158μm, [O I] 63μm, [O III] 88μm, and [N II] 122 μm fine-structure lines in star-forming regions of five galaxies from the LITTLE THINGS sample: DDO 69, DDO 70, DDO 75, DDO 155, and WLM. All four lines were observed for each galaxy, with the single exception of DDO 75, which had no [O III] observation. A summary of the observations is given in Table 2. The map regions were observed with a chopping/nodding raster pattern in the Open Time 1 (OT1) mission phase over a total of 53 hours. Observed lines are not spectrally resolved, with the velocity FWHM ranging from roughly 90 km/s for the [O I] 63μm line to 240 km/s for the [C II] 158μm line.

The line maps in each galaxy were observed using 2×2 rasters of 4.″5 point and line steps for both the "blue" and "red" arrays. All observations were performed in the chop-nod mode with a large off-source chop throw of 6′, sufficiently far away from any galactic star-forming regions. The total field of view covered for each galaxy is 51.″5 per side – the sum of the PACS grid of 5×5 spatial pixels (referred to as *spaxels* in the *Herschel* community) spanning 9.″4 on each side, plus the raster step.

2.2. *Reduction*

Basic data reduction was performed using the *Herschel* Interactive Processing Environment v11.1.0 (HIPE; Ott 2010) with calibration tree 56. The HIPE ChopNod LineScan pipeline was used to calibrate flux and wavelength, as well as mask bad pixels – those that are outliers, glitches, saturated, or noisy – resulting in "Level 1"

(B) But the lines are not spectrally resolved, so a sentence stating what the cube is good for will clear up confusion.

TABLE 2
OBSERVATIONS

Galaxy	Line	RA (J2000) (h m s)	DEC (J2000) (d m s)	OBSID	Date (YYYY-MM-DD)	Duration (s)	Field of View (pc per side)
DDO 69	[C II]$_{\lambda158}$	09 59 33.37	+30 44 37.63	1342232282	2011-11-12	4612	200
	[O I]$_{\lambda63}$	09 59 33.32	+30 44 36.18	1342232283	2011-11-12	8380	
	[O III]$_{\lambda88}$	09 59 33.02	+30 44 27.35	1342232284	2011-11-12	1787	
	[N II]$_{\lambda122}$	09 59 33.39	+30 44 38.15	1342232312	2011-11-13	23,684	
DDO 70	[C II]$_{\lambda158}$	09 59 58.20	+05 19 40.07	1342233705	2011-12-06	4612	325
	[O I]$_{\lambda63}$	09 59 58.15	+05 19 38.44	1342233706	2011-12-06	8380	
	[O III]$_{\lambda88}$	09 59 57.89	+05 19 29.71	1342233707	2011-12-06	1787	
	[N II]$_{\lambda122}$	09 59 58.19	+05 19 39.83	1342233708	2011-12-06	23,684	
DDO 75	[C II]$_{\lambda158}$	10 11 06.13	-04 42 23.29	1342232588	2011-11-21	4612	325
	[O I]$_{\lambda63}$	10 11 06.09	-04 42 24.95	1342232589	2011-11-21	8380	
	[O III]$_{\lambda88}$	...	...	...	...	...	
	[N II]$_{\lambda122}$	10 11 06.13	-04 42 23.55	1342232590	2011-11-21	23,684	
DDO 155	[C II]$_{\lambda158}$	12 58 40.10	+14 12 56.86	1342236274	2012-01-03	4612	549
	[O I]$_{\lambda63}$	12 58 40.09	+14 12 56.63	1342236275	2012-01-03	8380	
	[O III]$_{\lambda88}$	12 58 39.82	+14 12 47.87	1342236276	2012-01-03	1787	
	[N II]$_{\lambda122}$	12 58 40.13	+14 12 58.02	1342236277	2012-01-04	23,684	
WLM	[C II]$_{\lambda158}$	00 02 01.62	−15 27 51.42	1342236873	2012-01-08	4612	250
	[O I]$_{\lambda63}$	00 02 01.63	−15 27 51.63	1342237491	2012-01-14	8380	
	[O III]$_{\lambda88}$	00 02 01.40	−15 27 40.50	1342236874	2012-01-08	1787	
	[N II]$_{\lambda122}$	00 02 01.63	−15 27 51.87	1342236282	2012-01-04	23,684	

(5) cubes. We utilize two sets of final projected data products for our analysis: 3-dimensional data cubes, which contain spectral information in addition to spatial information; and 2-dimensional integrated flux maps.

The 2D images for each of the observed lines were created using the PACSman package (Lebouteiller, et al. 2012), which is a suite of utilities for line-fitting, mapping and analyzing *Herschel* data that have been calibrated and masked by HIPE. Normally within HIPE, a spectrum for each of the 25 spaxels is created by rebinning the calibrated and masked data "cloud" of up to several hundred thousand readouts in each spaxel. From there, the user can perform line fits and integrate fluxes with their preferred tasks. This process can average out much of the spatial and spectral information available in the data before fitting, such as minor dithers in the RA and DEC of nod positions and slight spatial dependences of spectral layers in the cubes, which can result in a reduction of the dynamic range of the final images. In PACSman, by contrast, Gaussian-plus-polynomial profiles are fit to the full data cloud of line-plus-continuum emission at each spaxel in each raster position, utilizing all available information, without prior rebinning. Fits to some sample spectra of our observed fine-structure lines are shown in Figure 2.

We utilize the Monte Carlo option to robustly estimate the fit errors. PACSman does this by iteratively adding random perturbations to the spaxel data cloud values and fitting the shocked data. First, the data for a spaxel are binned, and the error attributed to the individual points in a bin is the standard deviation of the values contained within. Then this error is used as the dispersion (σ) in a normal distribution to generate the perturbation for a given data point. The final error is taken to be the standard deviation of the distribution of fit results from the perturbed flux arrays. Tests on several maps determined that 400 iterations was the optimal number to produce stable and reasonable error estimates that do not differ significantly from those produced by higher iteration values.

To produce the final maps, PACSman uses an approach to map projection similar to Drizzle (Fruchter & Hook 2002), where the rasters are projected onto a sub-spaxel grid of ∼3″pixels. The value at each projected pixel is determined from the corresponding spaxel fraction, assuming uniform surface brightness in each spaxel. Thus, each pixel in the final projection grid can correspond to several line fits, which are weighted and averaged to make the resulting 2D flux maps (see Figures 1, 6, 3, 11, and 12).

The 3D cubes are called `slicedProjectedCubes` in the HIPE parlance, and are the final products from the pipeline. All of the spectral data, initially organized in sets of 5×5 spaxels, are projected onto a grid of smaller pixels. Where PACSman projects fitted fluxes, however, HIPE projects the rebinned spectra directly, resulting in spatial maps of uniformly binned spectra.

PACSman can give more reliable fitted fluxes for given pixels, for the reasons mentioned above, and the superior dynamic range of the these maps aids in comparing different regions within the image. However, the preservation of spectral information is crucial for some applications. Pixel errors can be quite large for faint real flux, so stacking the spectra from the 3D maps directly over an area of interest before fitting can provide better *integrated* signal to noise for an extended region. While integrated fluxes of the bright [C II] line are roughly the same using both data products, the 3D spectral cubes are better for characterizing the integrated emission from the other three lines in our galaxies. To summarize: in our low surface-brightness regime, the PACSman maps provide better morphological and qualitative information, while the 3D cubes give better integrated fluxes. Spectrum stacking is discussed in more detail in § 3.1.

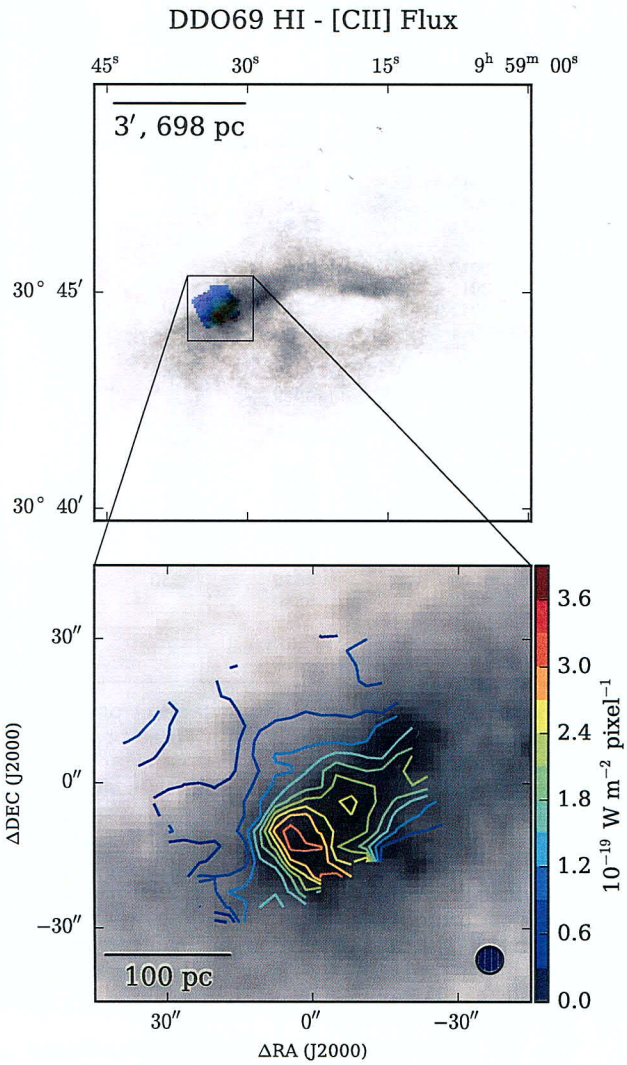

FIG. 1.— Overlay of *Herschel* [C II] contours onto H I in DDO 69. The [C II] beam is shown in the lower frame. Overlays of the other galaxies can be found in Figure 11 of the online edition.

2.3. *Ancillary Data*

Three of our five galaxies – DDO 69, DDO 70, and DDO 75 – were observed with the PACS and SPIRE photometers aboard *Herschel* during OT2. The final maps were made with the Scanamorphos package (Roussel, H. 2013). The full discussion of the *Herschel* photometry data reduction will be covered in our upcoming paper (Cigan, et al., in prep.). The resolution of these data are closely matched to the spectral observations, and so they are preferable in calculations of TIR for comparisons with the spectral lines.

All five of our galaxies were mapped in 24, 70, and 160μm continuum with the *Spitzer Space Telescope* and presented by Dale, et al. (2009) as part of the *Spitzer* Local Volume Legacy Survey. A search with the NASA Extragalactic Database (NED) reveals IRAS 60μm and 100μm measurements for three of our galaxies: DDO 70 (Lisenfeld, et al. 2007), DDO 75 (Moshir, et al. 1990), and WLM (Rice, et al. 1988).

We use the B-band images obtained by Hunter & Elmegreen (2006) for FIR/B ratios. These maps, originally in units of counts, are first converted to units of luminosity using the distances listed in Table 1 before integration. The total uncertainties reported combine overall systematic errors with internal errors given by the error maps of each galaxy.

We use the LITTLE THINGS maps of the neutral hydrogen (H I) content in these galaxies, which are based on Very Large Array (VLA) observations in B-, C- and D-configurations. The H I maps have a common angular resolution of 6″. The data were presented by Hunter, et al. (2012) and can be downloaded from the LITTLE THINGS NRAO science web page [5].

In our line ratio maps, we make use of the data points presented by Hunter, et al. (2001, hereafter H+01) for observations of other LITTLE THINGS galaxies with *ISO* and *IRAS*, as well as data for a variety of other galaxy types presented by Brauher, et al. (2008, hereafter B+08) and references therein. The IRAS 60/100μm values for DDO 69 and DDO 155 were not reported in those studies, and we take their values from the following additional sources. Fluxes and uncertainties for DDO 69 60μm, DDO 69 100μm, and DDO 155 60μm measurements come from Tacconi & Young (1987). The same authors only report an upper limit for the 100μm flux in DDO 155, while Melisse & Israel (1994) report a flux detection without an accompanying uncertainty. For this source, we use the published detection as the flux, and take the 1σ upper limit as the uncertainty.

2.4. *Convolving the Data*

When comparing data with different resolutions, it is essential to convolve the pertinent maps to a common beam resolution to ensure that the results are valid. Here "beam" is the commonly used term in the radio community meaning the resolution element, or point-spread-function (PSF). "Beam size" refers to the PSF Full-Width-at-Half-Maximum (FWHM). Comparisons of the PACS [O I] and [O III] maps with each other require no further processing, as they have a common beam size of ∼9.″5 FWHM (Poglitsch, et al. 2010), though comparisons with [C II] maps require smoothing to the 157μm beam size of 11.″5. The *Spitzer* maps each have different resolutions. We use the values reported by Aniano, et al. (2011) for the *Spitzer* beams. Table 3 lists the beam sizes of each instrument. The MIPS 160μm beam is on the order of the entire PACS field-of-view. Any small resolved aperture within a *Herschel* map will thus be on the order of (or smaller than) the MIPS_{160} beam, so we make no spatially resolved comparison between the two instruments on those scales. All *Spitzer* maps are convolved to the common beam size of 38.″8 FWHM before quantifying values for the TIR continuum.

3. ANALYSIS

There are several qualitative characteristics of our line maps that immediately stand out. All observations exhibit, in general, very low surface brightness (typical "detection" S/N is ∼3-5 for [O I], [O III], and [N II], with

[5] http://science.nrao.edu/science/surveys/littlethings

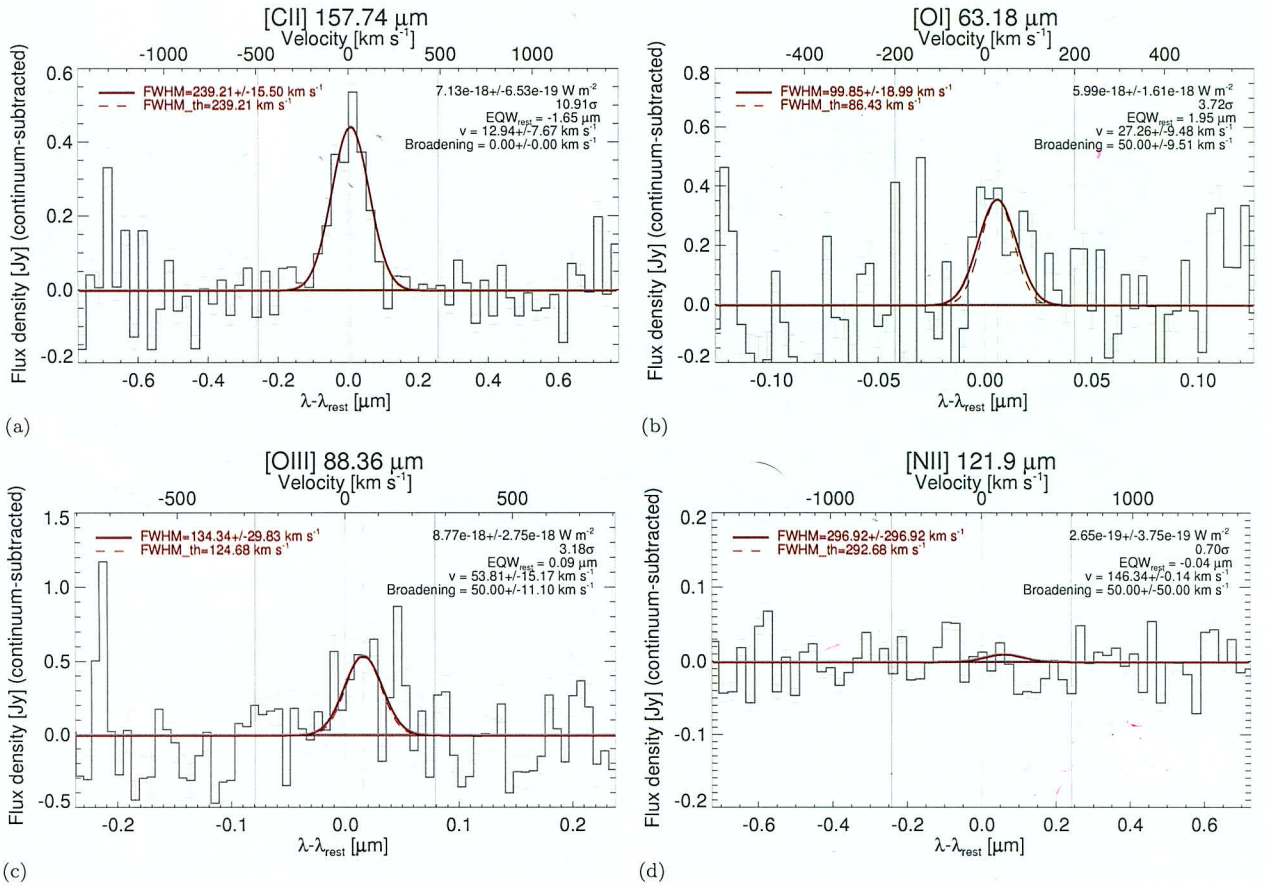

FIG. 2.— Sample continuum-subtracted spectra from single rasters of the central spaxel in the PACSman fit procedure for DDO 155. It is obvious from these independent observations of the same target that while there is [C II], [O I], and some [O III] emission, there is no cospatial [N II] signal in this particular region. FWHM_{th} is the expected (minimum) line width, due to the thermal properties of the instrument. Broadening is the excess line width beyond FWHM_{th}, when added in quadrature. That is, $\mathrm{FWHM}^2 = \mathrm{FWHM}^2_{th} + \mathrm{Broadening}^2$. EQW_{rest} is the width in wavelength units for which a box defined from zero flux to the continuum level, and centered at the rest wavelength, has an area equal to that of the integrated flux.

TABLE 3
Herschel AND *Spitzer* INSTRUMENT PARAMETERS

Instrument	Band	Beam Size (FWHM)	Calibration Uncertainty
PACS	[C II]	11.″5	12%
PACS	[O I]	9.″5	11%
PACS	[O III]	9.″5	12%
PACS	[N II]	10.″0	12%
MIPS	24μm	6.″5	4%
MIPS	70μm	18.″7	10%
MIPS	160μm	38.″8	12%

REFERENCES. — Beam sizes come from Poglitsch, et al. (2010) (PACS) and Aniano, et al. (2011) (*Spitzer* MIPS). Instrumental calibration uncertainties are as follows. PACS: The PACS Obersvers' Manual [a]; MIPS 24μm: Engelbracht, et al. (2007); MIPS 70μm: Gordon, et al. (2007); MIPS 160μm: Stansberry, et al. (2007).

[a] `http://herschel.esac.esa.int/Docs/PACS/html/pacs_om.html`

a typical brightness of $\sim 10^{-9}$ W m^{-2} sr^{-1}), though [C II] emission is brightly detected in all five galaxies (maximum pixel S/N ~10-30). While some targets show enhanced [C II] flux in certain resolved regions, there is generally emission extended over the majority of each image. The [O I] and [O III] emission is, on average, spotty at best. The [N II] detections in our maps are marginal, though this result is not entirely unexpected, since [N II] is usually fainter than the other FIR lines in galaxies.

There are often bright spots at the edges of the images. An inspection of the lines and fits in the cubes reveals that this is usually not real emission; reduced coverage can skew the averages, but the errors are correspondingly high. We generally ignore the noisy outer edges of the maps and consider only the bright regions in the interior. One notable exception is the southwest corner of the DDO 155 [C II] map (see Figure 3), which shows some emission that is cospatial with a region of high-density neutral hydrogen, V-band, FUV, Hα, and 160μm signal. DDO 69 displays a bright knot of [N II] in the southwest corner of the image (Figure 12) that is cospatial with 160μm emission and between clumps of V, FUV, and Hα. However, only one raster registered a detection of 3.72σ amid much noise, while it is not detected in the other rasters.

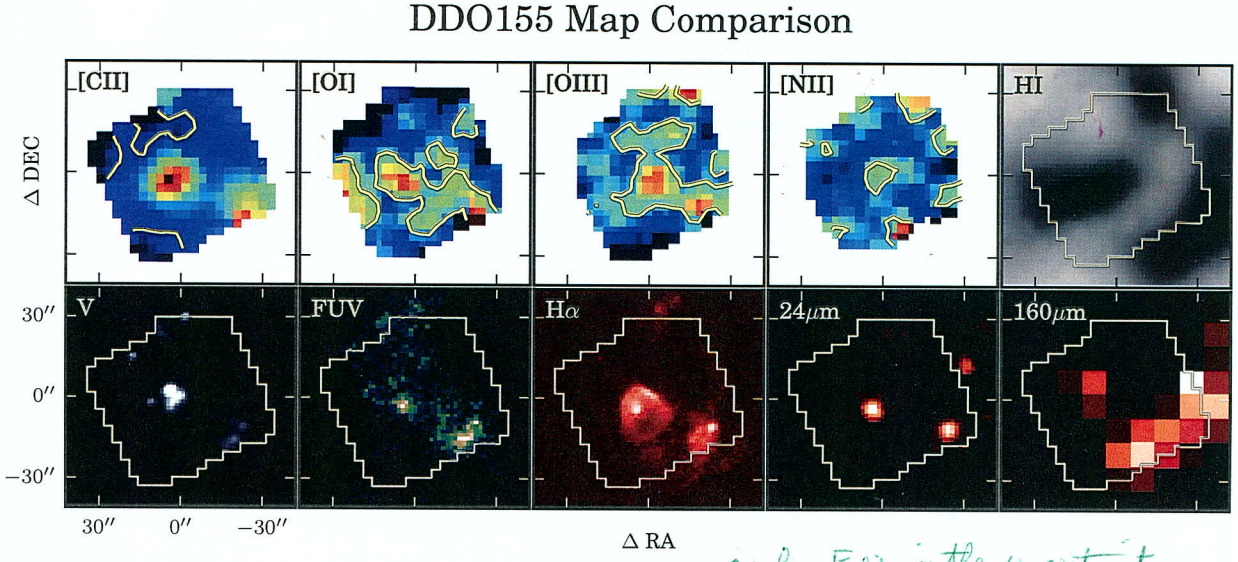

FIG. 3.— Spatial comparison of emission in the *Herschel* maps with other observations at several wavelengths. DDO 155 appears here, with the other galaxies available in the online edition. Each image scaling is independent, to enhance dynamic range and draw out faint features. The *Herschel* maps have contours showing where pixel $S/E_{fit} > 1$. This low cutoff for *pixel* S/N indicates true areas of emission fairly well - we are interested in detections aggregated from *regions* the size of one beam or larger. In the other maps, the white outlines indicate the footprint of the [C II] map. Here, H I is from Hunter, et al. (2012), V-band from Hunter & Elmegreen (2006), FUV from Dale, et al. (2009), Hα from Hunter & Elmegreen (2004), 24μm & 160μm from Dale, et al. (2009).

3.1. *Stacking spectra*

Due to the faint nature of our targets, we must be very careful about the details of flux integration. Fitting a flux to each pixel's spectrum before summing spatially is perfectly reasonable for high signal-to-noise observations, but can miss much of the faint and diffuse emission. If the line-of-sight signal is on the order of the noise, when the fitted fluxes are summed, the result will basically be a sum of the pixel noise values. However, if the line-of-sight spectra are first stacked over some spatial region before being fit, the true noise will tend to average out, while any real signal will compound to reveal a much clearer peak. After stacking, the flux can be determined from a line profile fit as usual to provide a more robust estimate of the signal and noise in that region. This spectral stacking technique gives much better results in our low surface brightness regime.

We provide fluxes determined by stacking all spectra in each spectral cube, over the whole field of view. While the [C II] line is well-detected in all our galaxies, the other line maps still give some non-detections when stacked over the whole cube, especially for [N II] and [O III]. Exploring these spectral maps by hand shows that there are indeed regions of detectable flux in many of these targets where the lines were not detected globally, meaning that real emission is restricted to small areas, and the other lines of sight only contribute noise, which washes out the signal.

To address this, we identify smaller individual regions in each map where there are traces of real emission. These specific regions are shown for each map in Figure 4. The resulting fluxes from these regions are shown in Figure 5.

3.2. *TIR vs. FIR*

Some care must be taken with definitions of "Far"- and "Total"-Infrared emission (FIR, TIR, respectively), as there is some overlap in the literature. In general, FIR is taken to be the range from several to some hundreds of microns, while TIR covers the range from several to a roughly a thousand microns; the devil is in the details. For example, Hollenback & Tielens (1997) use FIR to refer to the total far-IR dust continuum intensity, without stating concrete bounds, though 1-1000μm and the *COBE* 4-1000μm ranges are mentioned in passing. Another common definition for TIR is 3-1100μm (Dale, et al. 2001). The typical range used for FIR is 42.25-122.25 (Helou, et al. 1988), commonly shortened as 42-122 Dale, et al. (2001, e.g.,) or 40-120μm Hunter, et al. (2001, e.g.,). More recently, Rémy-Ruyer, et al. (2013) have used 50-650μm for FIR to reflect the spectral coverage of the *Herschel* photometers. Some of these differences may be minor, but even small offsets of integration boundaries can affect resulting fluxes noticeably when explicitly summing SEDs of objects at these temperatures. Furthermore, it is critical to compare like with like in order to get meaningful results.

FIR has traditionally been preferred to TIR for characterizing the infrared continuum, for various reasons including the lack of instruments able to sample the longer wavelengths of the IR spectrum. This was reasonable because observation targets were typically bright with thermal radiation that covered the FIR ranges well. However, the narrow band of the canonical FIR can be a poor match for the SEDs of cooler objects – a simple blackbody spectrum at 25K peaks just near the edge of the range. We use TIR in our analysis to better represent the majority of the emission in infrared continuum. We determine TIR luminosities for all of our galaxies from a combination of *Spitzer* MIPS measurements at 24,

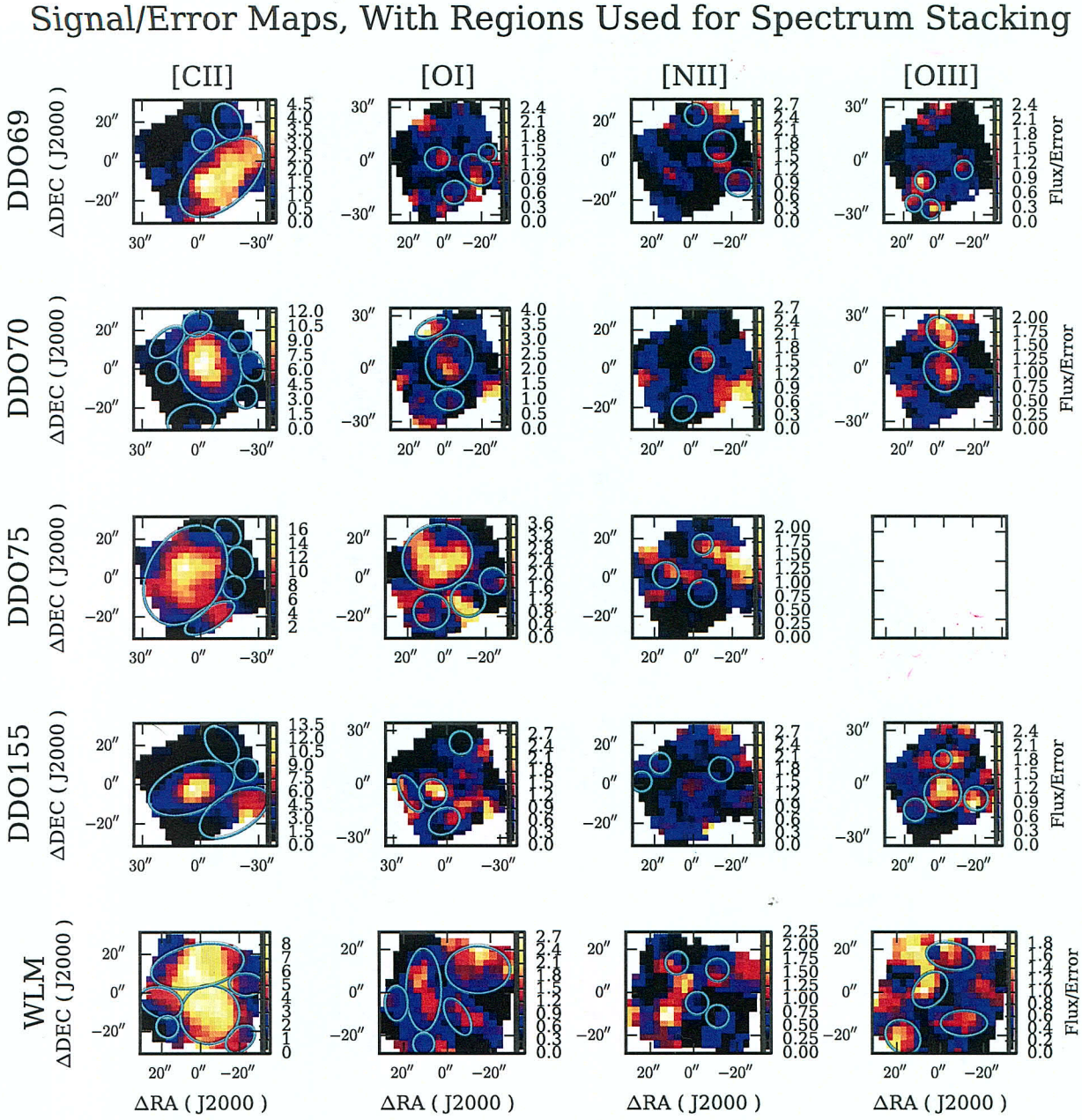

FIG. 4.— PACSman integrated flux signal-to-error maps for our galaxies. The cyan ellipses are the regions used for spectral stacking, based on signal found by manual inspection of the 3D spectral cubes. Note that several regions of manually-identified signal do not overlap exactly with the bright spots from the integrated flux maps. This is especially true for the [N II] maps, for which the emission is particularly faint.

70, and 160 μm, and we also calculate TIR from PACS 100μm for our three galaxies that have these data.

H+01 and B+08, following the earlier definition of Helou, et al. (1988), express IRAS far-infrared flux as $\mathrm{FIR} = 1.26\times10^{-14}[2.58f_\nu(60\mu m)+f_\nu(100\mu m)]$ W m^{-2}, where f_ν is in Jy, to characterize the spectrum from 40-120μm based on those two fluxes. H+01 and Dale, et al. (2009), following Dale & Helou (2002), estimate the TIR from 3-1100μm as $f(\mathrm{TIR})_{IRAS} = 2.403(\nu f_\nu)_{25\mu m} - 0.2454(\nu f_\nu)_{60\mu m} + 1.6381(\nu f_\nu)_{100\mu m}$ and $f(\mathrm{TIR})_{MIPS} = 1.559(\nu f_\nu)_{24\mu m}+0.7686(\nu f_\nu)_{70\mu m}+1.347(\nu f_\nu)_{160\mu m}$. See §5.2 of Dale, et al. (2009) for further discussion.

Draine & Li (2007) use the 8, 24, 70, 160 micron data from IRAC and MIPS to estimate the TIR luminosity: $\mathrm{L_{TIR}} = 0.95\langle\nu\mathrm{L}_\nu\rangle_{7.9} + 1.15\langle\nu\mathrm{L}_\nu\rangle_{24} + \langle\nu\mathrm{L}_\nu\rangle_{71} + \langle\nu\mathrm{L}_\nu\rangle_{160}$. We only have 8$\mu$m maps for DDO 69 and DDO 155; therefore, in the interest of consistency, we use the definition of Dale & Helou (2002) for all five galaxies. For our

$f(\mathrm{TIR})_{MIPS}$ from

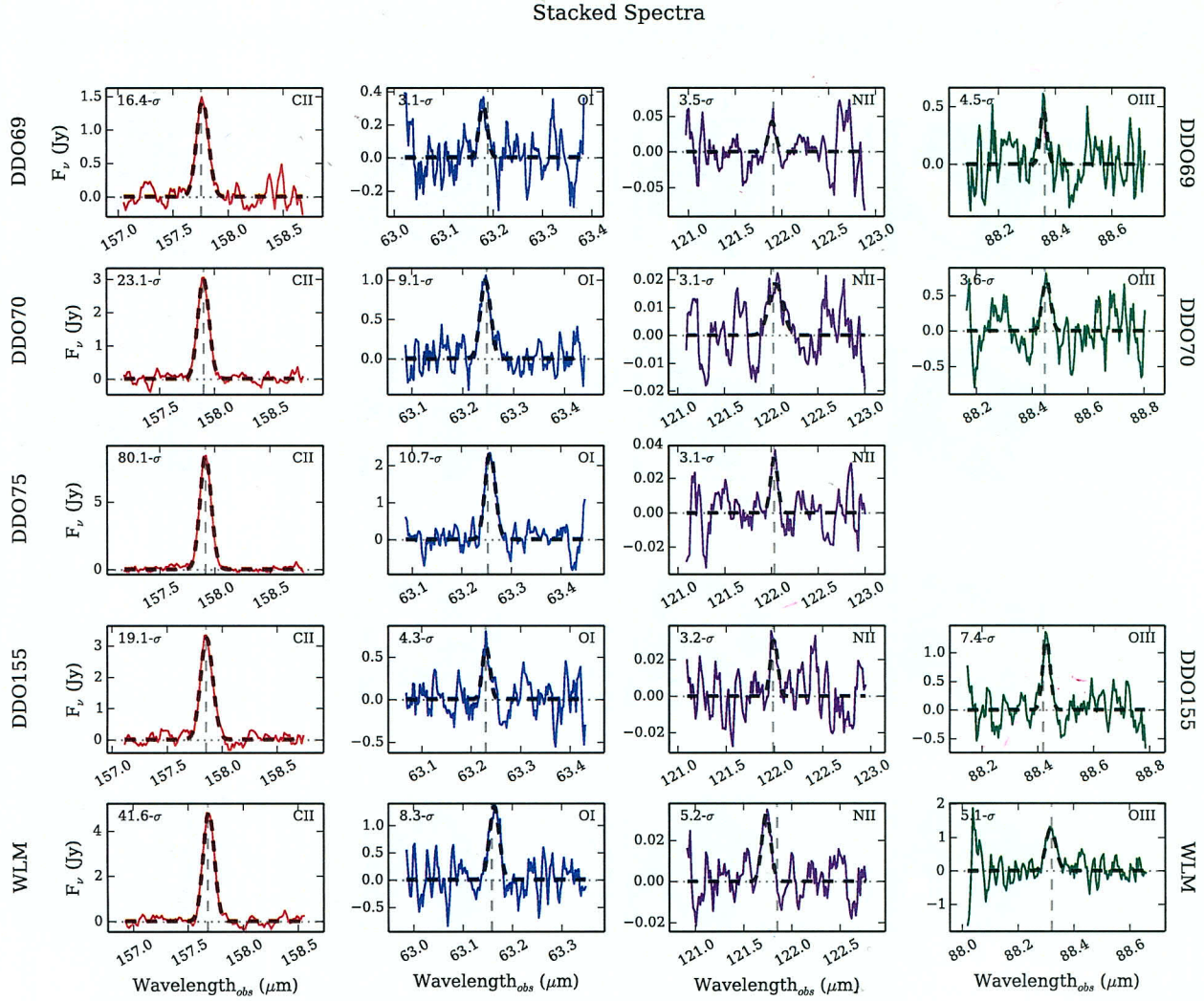

FIG. 5.— Spectra from the regions described in Figure 4 are stacked to give a global measure of all observed flux. The vertical dashed grey line indicates the expected line center location, based on the bulk velocity of the galaxy.

sources with *Herschel* photometry, we also estimate TIR using the prescription of Galametz, et al. (2013) based on PACS 100μm: $\log(L_{TIR,100\mu m}) = (1.0\times)\ \log(\nu L_\nu) + 0.256$, where L_{TIR} and νL_ν are in units of $L_\odot$.

While we only use TIR in our line ratios, we do use FIR for comparing to literature values of FIR/B. H+01 compared FIR (*IRAS* 60μm and 100μm estimate of 40-120μm) and TIR (*Spitzer* 24μm, 70μm, and 160μm estimate of 3-1100μm) measurements for five dwarfs, finding that $L_{TIR} = 1.9 - 2.2\times L_{FIR}$ in each case. There exist IRAS measurements for our sample from which to calculate L_{FIR}. However, since the resolution of IRAS is much larger than our *Herschel* fields of view, they would only serve as broad averages, and may not reflect well upon the smaller-scale environments. Instead, we rely on our *Herschel* photometry, fitting modified blackbodies in the manner described by Rémy-Ruyer, et al. (2013), and directly integrate the spectra over the TIR and FIR ranges, over the areas encompassed by reliable [C II] emission. The average TIR/FIR value from those three galaxies – 1.63 ± 0.41 – is used for DDO 155 and WLM.

3.3. *Flux Integration Scales*

In order to look at several emission features on different scales, we sum the flux at each wavelength in several ways. The first scale is that of the entire field of view of the PACS images, listed in Table 2. Each map includes several lines-of-sight with high noise and poor detections, particularly around the image edges. As a result, these total sums are not a reliable measure of the real emission in the observed maps, but they are nonetheless listed along with our other flux measurements in Table 4 for completeness.

Next, we combine all individual spectra from regions of the maps with faint signal to produce global stacked spectra. This is useful for drawing out the faint signals which would otherwise be averaged out by noise. The resulting spectra can tell us about the bulk average properties of emission in a particular map. For the most general treatment, we define elliptical regions that contain be-

lievable signal, based on manual inspection of the data cubes. It should be noted that many of the regions with detectable stacked signal are offset from the brightest regions in the PACSman maps. Each region is no smaller than the limiting beam size for that map. All the spectra from a selected region are then stacked, and a line is fit to determine the integrated flux. These measurements are listed in Table 4, and the regions used are shown in Figure 4. This can be taken to be the "total" source flux observed in each map. When comparing *Herschel* line fluxes to *Spitzer* FIR, we first smooth all pertinent data to the resolution of the MIPS 160μm map, which has the coarsest resolution. The TIR values reported are for the entire PACS field of view.

To pinpoint distinct features on resolved scales, we repeat this stacking procedure, but now for each individual selected region separately. For line-line ratios, we stack spectra using the region of the line that typically has the limiting flux. For example, the [O III] line generally has a smaller area of real emission than the [C II] line, so we use each [O III] region to stack the spectra and determine fluxes. That is, we use the same [O III] region for stacking both the [O III] and [C II] spectra, so that the line ratios are covering the exact same areas. Since the region sizes are much smaller than the MIPS 160μm beam, a comparison of these values with $\mathrm{TIR}_{Spitzer}$ would not be valid. Instead, we consider only TIR from our PACS photometry, available only for DDO 69, DDO 70, and DDO 75.

Finally, to make an objective set of measurements for comparison, we investigate line ratios on a beam-by-beam basis, as opposed to manually selecting regions of interest. 25 uniform regions were created in a grid, each the size of one [C II] beam to ensure independent measurements. Ratios were then computed for each region in the new grid. We again make no comparison of the *Herschel* lines with *Spitzer* TIR fluxes at this scale – several [C II]-beam-sized pixels fit within the limiting 160μm beam – but we use the PACS TIR where available.

3.4. *Errors and Uncertainties*

Since our targets are extended with extremely low surface brightness, we rigorously examined the internal uncertainties related to our measurements to ensure that they are reliably characterized; conservativism in error estimation is especially prudent in the low-S/N regime. The two types of error we discuss below are the statistical error in the spectral fits and the general instrumental uncertainty of order 12%.

For stacked spectra, the fit error is the formal uncertainty on the area under the gaussian with independently fitted parameters A, x_c, and σ:

$$\Delta^2_{fit} = \mathrm{Flux}_{fit} \cdot \sqrt{\left(\frac{\epsilon_A}{A}\right)^2 + \left(\frac{\epsilon_{x_c}}{x_c}\right)^2 + \left(\frac{\epsilon_\sigma}{\sigma}\right)^2}$$

Typical values for the stacked spectra fit errors are around 10%. The errors used for the S/N ratios in the PACSman maps (Figures 3, 4, 6, 12) are the individual projected pixel errors.

When comparing measurements from different instruments, we must include the uncertainty arising from overall instrumental effects. The "internal" uncertainties described above and those due to the system as a whole add in quadrature. The systematic uncertainties for the PACS Spectrometer and the *Spitzer* MIPS bands are summarized in Table 3. The sum total uncertainty for a specific integration region combines the summation (fit) error and the systematic error, which we compute as $\Delta_{\mathrm{tot}} = \sqrt{\Delta^2_{fit} + \Delta^2_{sys}}$.

3.5. *Results of Flux Integrations*

We note that there is generally not widespread reliably-detected [O I], [O III], and [N II] line emission in our galaxies. Perhaps there is a relatively low abundance of these species in our systems due to metallicity or other compositional effects. Alternatively, the local conditions in these galaxies may simply not be ripe for strong emission from these lines. For nitrogen, the majority of the species in these regions may be in the neutral phase, with little ionizing radiation above 14.53 eV. However, the Hα maps show that there are H II regions within each *Herschel* footprint, and we expect that any nitrogen in H II regions should be in the ionized phase. Cormier, et al. (2012) recently published FIR line fluxes for Haro 11, finding [N II]/[C II] $\simeq$ 0.04, and the handful of galaxies in the Dwarf Galaxy Survey (DGS; Madden, et al. 2013) where [N II] was detected have ratios of about 0.02.

The IRAS observations of NGC 1156, NGC 1569, and IC 4662 discussed by H+01 provide only upper limits to [N II] fluxes, giving similar [N II]/[C II] ratios between 2-8% for those dwarfs. Assuming that our galaxies follow this trend, this implies that our [N II] integration times – though 6.5 hours per pointing, or roughly five times the length of the [C II] observations – were still not long enough to detect the weak 122 μm emission. On the other hand, our results could simply be evidence that the diffuse ionized phase did not make up a large portion of our observed regions, which would indicate that the majority of the [C II] in these regions originates in PDRs, as opposed to the diffuse ionized phase.

The [N II] detection in WLM has the highest statistical significance in our sample – it is the only one over 5σ. The emission has an offset of roughly -260km/s from the galaxy bulk velocity, however, which complicates matters. One explanation could be that it may be due to a supernova remnant, though nothing appears at those coordinates in the LITTLE THINGS radio continuum maps (Kitchener, et al., submitted). Regardless, the [C II], [O I], and [O III] emission in WLM is centered at the galaxy's recessional velocity, which means that these lines might not originate in the same physical location as the [N II].

3.6. *Flux Ratios*

Figure 7 shows ratios of the various *Herschel* bands compared to metallicity and the common FIR diagnostics $f_{60\mu m}/f_{100\mu m}$ and L_{FIR}/L_B for our sample. Figure 8 shows ratios of *Herschel* lines to L_{TIR} compared with $f_{60\mu m}/f_{100\mu m}$, L_{FIR}/L_B, and metallicity. Figures 9 and 10, in comparison, shows the *Herschel* line ratios in comparison to L_{TIR} and L_{TIR}/L_B for smaller-scale resolved regions within each galaxy.

When computing ratios of *Herschel* and *Spitzer* fluxes, special care must be taken for integration regions that approach the size of the MIPS 160μm pixels, which are the largest in our sample, at 9″. For all comparisons of the resolved regions between the two instruments, we

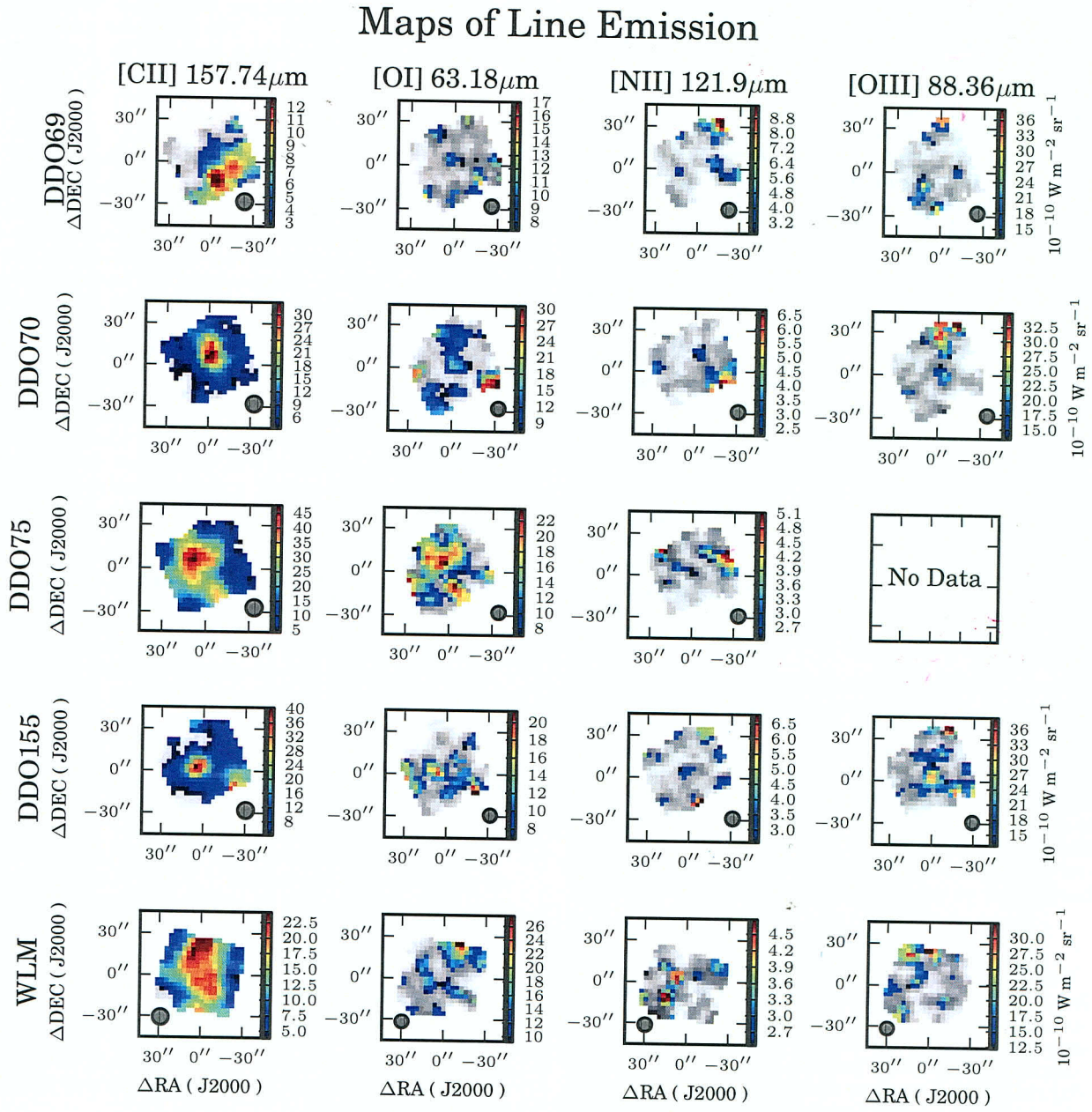

FIG. 6.— PACSman flux maps of the four observed lines in each of our five galaxies. Pixels where the signal-to-error ratio is less than 1 appear in grayscale. The colorscale shows the brightness values of these remaining pixels. Regions where there are several pixels clumped together (on the order of a beam area) and brighter than the darkest blue generally indicate where the real detections are. This breaks down for the very faint diffuse emission, however, as demonstrated for the [N II] line. The striped circle at the bottom of each map shows the PACS beam size of the given line.

regrid the [C II], [O I], 24μm and 70μm maps, which were previously convolved with a custom kernel to the same Gaussian beam, to a uniform pixel size of 9″before integrating the flux – this ensures we are using equivalent regions in each map.

The 60μm/100μm ratio is a diagnostic of the dust-heating intensity in a system. This FIR color is often taken to be a proxy for dust temperature, and is typically associated with global star formation activity (Dale, et al. 2001). The ratio of FIR and B luminosities represents the amount of light reprocessed by dust in the system compared to the starlight that escapes. It is typically taken as an indicator of both star formation activity and optical extinction.

When comparing the *Herschel* line fluxes with FIR emission from *Spitzer*, we estimate total uncertainties by adding the internal uncertainties within each image (§ 3.4) and calibration uncertainties from each instru-

TABLE 4
Integrated LINE FLUXES AND RATIOS ~~OVERALL~~

Quantity	DDO 69	DDO 70	DDO 75	DDO 155	WLM
			Spectral Stacking Over the All Pixels		
$f_{[C\ II]\lambda158}$ (10^{-17} W m^{-2})	2.31 ± 0.20	5.60 ± 0.27	14.30 ± 0.26	6.74 ± 0.47	9.27 ± 0.24
$f_{[O\ I]\lambda63}$ (10^{-17} W m^{-2})	(1.36)	3.44 ± 0.56	5.90 ± 0.59	1.70 ± 0.66	3.48 ± 0.68
$f_{[O\ III]\lambda88}$ (10^{-17} W m^{-2})	(5.43)	(3.31)	···	1.42 ± 0.56	6.71 ± 1.58
$f_{[N\ II]\lambda122}$ (10^{-17} W m^{-2})	(0.37)	(0.76)	(0.30)	(0.28)	(0.23)
			Stacking All Spectra from Selected Regions With Signal		
$f_{[C\ II]\lambda158}$ (10^{-17} W m^{-2})	2.35 ± 0.14	4.61 ± 0.20	12.84 ± 0.16	5.42 ± 0.28	7.35 ± 0.18
$f_{[O\ I]\lambda63}$ (10^{-17} W m^{-2})	0.49 ± 0.16	1.86 ± 0.20	4.48 ± 0.42	0.86 ± 0.20	2.50 ± 0.30
$f_{[O\ III]\lambda88}$ (10^{-17} W m^{-2})	0.53 ± 0.11	1.02 ± 0.28	···	1.59 ± 0.22	2.22 ± 0.43
$f_{[N\ II]\lambda122}$ (10^{-17} W m^{-2})	0.082 ± 0.023	0.069 ± 0.022	0.061 ± 0.019	0.059 ± 0.019	0.076 ± 0.015
			TIR and FIR		
$f_{TIR,Herschel}$, BB fit (10^{-15} W m^{-2})	1.39 ± 0.31	5.01 ± 0.79	9.29 ± 1.03	···	···
$f_{TIR,Herschel}$, PACS100μm (10^{-15} W m^{-2})	2.24 ± 0.45	7.67 ± 0.55	14.80 ± 0.67	···	···
$f_{TIR,Spitzer}$ (10^{-15} W m^{-2})	4.25 ± 1.20	15.36 ± 1.23	24.04 ± 0.98	7.92 ± 2.02	17.97 ± 1.57
TIR / FIR (*Herschel*)	1.87 ± 0.57	1.52 ± 0.34	1.49 ± 0.24	···	···
$f_{FIR,Spitzer}$ (10^{-15} W m^{-2})	2.27 ± 0.64	10.11 ± 0.81	16.13 ± 0.66	4.86 ± 1.24	11.02 ± 0.96
$f_{[C\ II]_{convolved}}$ (10^{-17} W m^{-2}) *	1.60 ± 0.12	4.16 ± 0.19	10.31 ± 0.14	4.71 ± 0.20	6.38 ± 0.13
$f_{[O\ I]_{convolved}}$ (10^{-17} W m^{-2}) *	(0.88)	2.48 ± 0.34	3.98 ± 0.35	1.25 ± 0.40	2.59 ± 0.38
$f_{[N\ II]_{convolved}}$ (10^{-17} W m^{-2}) *	(9.76)	(0.29)	(0.19)	(0.17)	(0.45)
[O I] / [C II] (10^{-2})	(25.45) ± 13.63	57.23 ± 8.87	36.95 ± 3.40	26.02 ± 8.07	36.69 ± 5.97
[N II] / [C II] (10^{-2})	(4.02) ± 3.98	(1.97) ± 1.39	(0.37) ± 0.54	(0.99) ± 1.39	(0.52) ± 1.09
[O III] / [C II] (10^{-2})	(29.52) ± 43.29	(4.71) ± 9.04	···	(21.44) ± 9.86	63.00 ± 10.94
[O III] / [O I] (10^{-2})	130.26	(13.57) ± 32.11	···	83.63 ± 46.30	192.69 ± 58.89
[C II] / $TIR_{Spitzer}$ (10^{-2})	0.38 ± 0.12	0.27 ± 0.05	0.43 ± 0.07	0.59 ± 0.17	0.35 ± 0.06
[O I] / $TIR_{Spitzer}$ (10^{-2})	(0.13) ± 0.08	0.16 ± 0.03	0.17 ± 0.03	0.16 ± 0.07	0.14 ± 0.03
[N II] / $TIR_{Spitzer}$ (10^{-2})	(0.0143) ± 0.7652	(0.0081) ± 0.0064	(0.0013) ± 0.0027	(0.0076) ± 0.0075	(0.0088) ± 0.0085
([O I] + [C II]) / $TIR_{Spitzer}$ (10^{-2})	0.51 ± 0.17	0.43 ± 0.07	0.59 ± 0.08	0.75 ± 0.22	0.50 ± 0.08
[C II] / $TIR_{Herschel,100\mu m}$ (10^{-2})	1.05 ± 0.22	0.60 ± 0.05	0.87 ± 0.04	···	···
[O I] / $TIR_{Herschel,100\mu m}$ (10^{-2})	0.22 ± 0.08	0.24 ± 0.03	0.30 ± 0.03	···	···
[N II] / $TIR_{Herschel,100\mu m}$ (10^{-2})	0.0367 ± 0.0050	0.0089 ± 0.0027	0.0041 ± 0.0004	···	···
([O I] + [C II]) / $TIR_{Herschel,100\mu m}$ (10^{-2})	1.27 ± 0.48	0.84 ± 0.12	1.17 ± 0.12	···	···
$f_{60\mu m}$ / $f_{100\mu m}$	0.333 ± 0.149	0.574 ± 0.121	0.379 ± 0.095	0.140 ± 0.300	0.308 ± 0.109
$L_{FIR,Spitzer}$ / L_B	0.018 ± 0.009	0.014 ± 0.005	0.125 ± 0.031	0.021 ± 0.009	0.025 ± 0.009
$L_{FIR,IRAS}$ / L_B	0.050 ± 0.011	0.024 ± 0.002	0.130 ± 0.016	0.011 ± 0.008	0.052 ± 0.009
$L_{FIR,Herschel100\mu m}$ / L_B	0.009 ± 0.003	0.006 ± 0.001	0.072 ± 0.012	···	···

NOTE. — Upper limits (3σ) are given in parentheses. When comparing [C II], [O I], and [N II] data with those from *Spitzer*, the *Herschel* data are first convolved to the beam size of the 160 micron map. These fluxes are noted with an asterisk (*).

ment (Table 3) in quadrature. The error is propagated in the standard manner for division.

3.7. *Spatial Comparison of FIR Line Emission*

We generally find that [O I] and [O III] emission are closely located to regions of [C II] emission, though they are not always precisely overlapping. Refer to Figure 6 for the flux maps of all five galaxies. In all five of our targets, the [N II] emission peaks are offset from the [C II] peaks. In all but DDO 75, for which the two peaks are offset by ∼15″, the brightest [N II] regions fall at the very edge of the main [C II] emission. This is a good indication that the bulk of the [C II] comes from PDRs instead of the diffuse medium in our objects.

DDO 69 has a bright [C II] peak in the south of the observed region, with emission extending to the south and west. The weak [O I] peak is roughly cospatial with the [C II], and the [O III] peaks 20″ to the east. DDO 70 peaks in [C II] in the center of the image, and is extended NE-SW. The [O I] emission again weakly peaks in the same region as the [C II], while the [O III] has one slight enhancement in the same position and another stronger one 30″ to the NW. DDO 75 has two bright regions visible in the [C II] map – one in the middle and one to the south. In each case, the [O I] peak is cospatial with the [C II], but the central [O I] knot is relatively thin in the N-S extent (∼10″), while maintaining the ∼25″ E-W extent of the [C II]. WLM shows a large, wide N-S column of [C II] spanning the entire map. The [O I] and [O III] peaks lie to the NW of the [C II] and are offset by ∼15″ from each other near the north edge of the footprint.

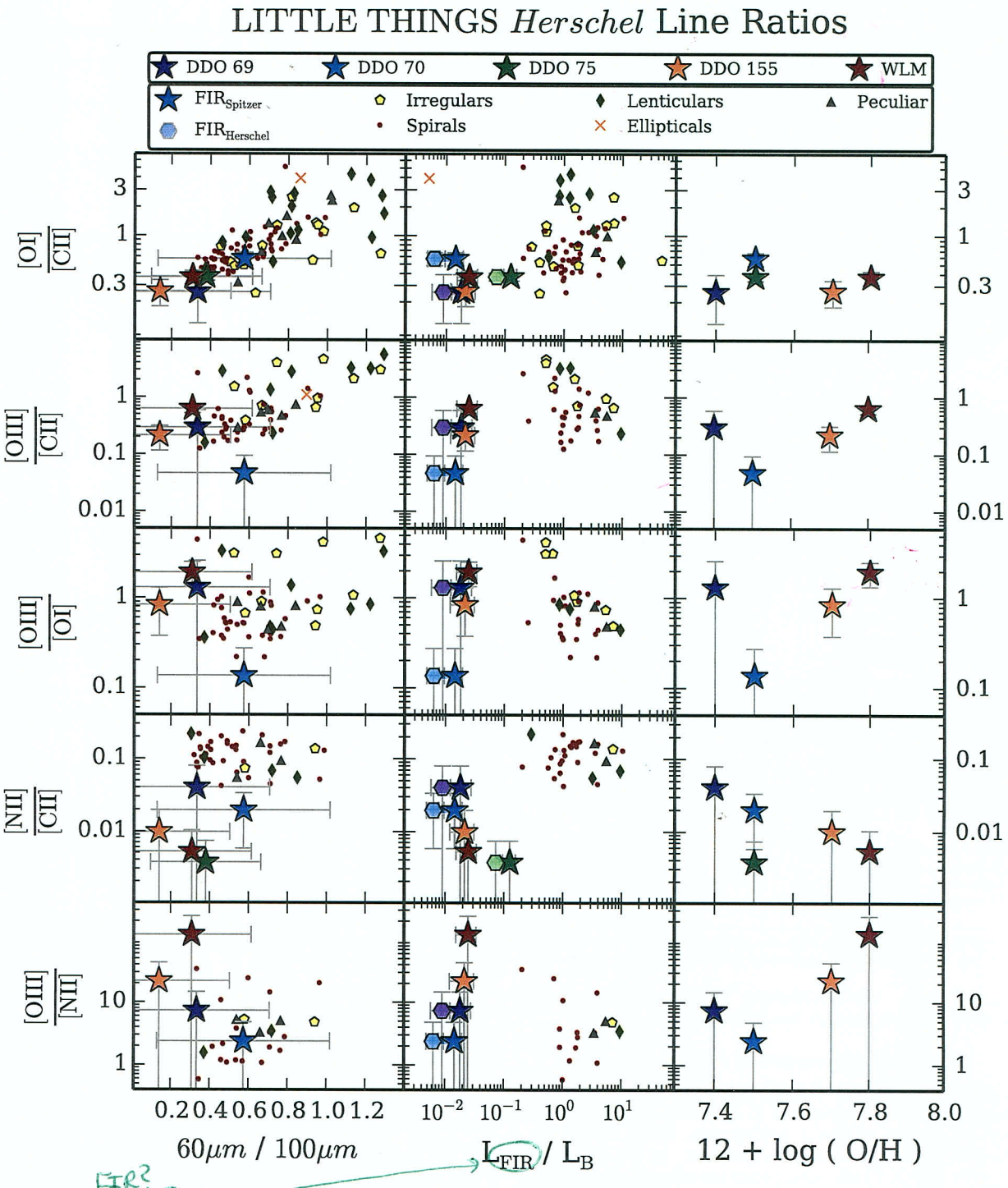

FIG. 7.— *Herschel* FIR line ratios. IRAS data for additional LITTLE THINGS galaxies come from Hunter, et al. (1989) and ISO data from Hunter, et al. (2001). Spiral, elliptical, and irregular galaxy data points from Brauher, et al. (2008) are given for comparison with the 60μm/100μm and FIR/B ratios. We only plot detections for the ~~background~~ data, omitting upper limits. For our measurements, detections are denoted by solid filled stars. Upper and lower limits (3σ) appear as empty stars with arrows the length of the uncertainty of that measurement. FIR derived from *Herschel* photometry is also shown for galaxies with PACS 100μm data: DDO 69, DDO 70, and DDO 75 (hexagon symbols).

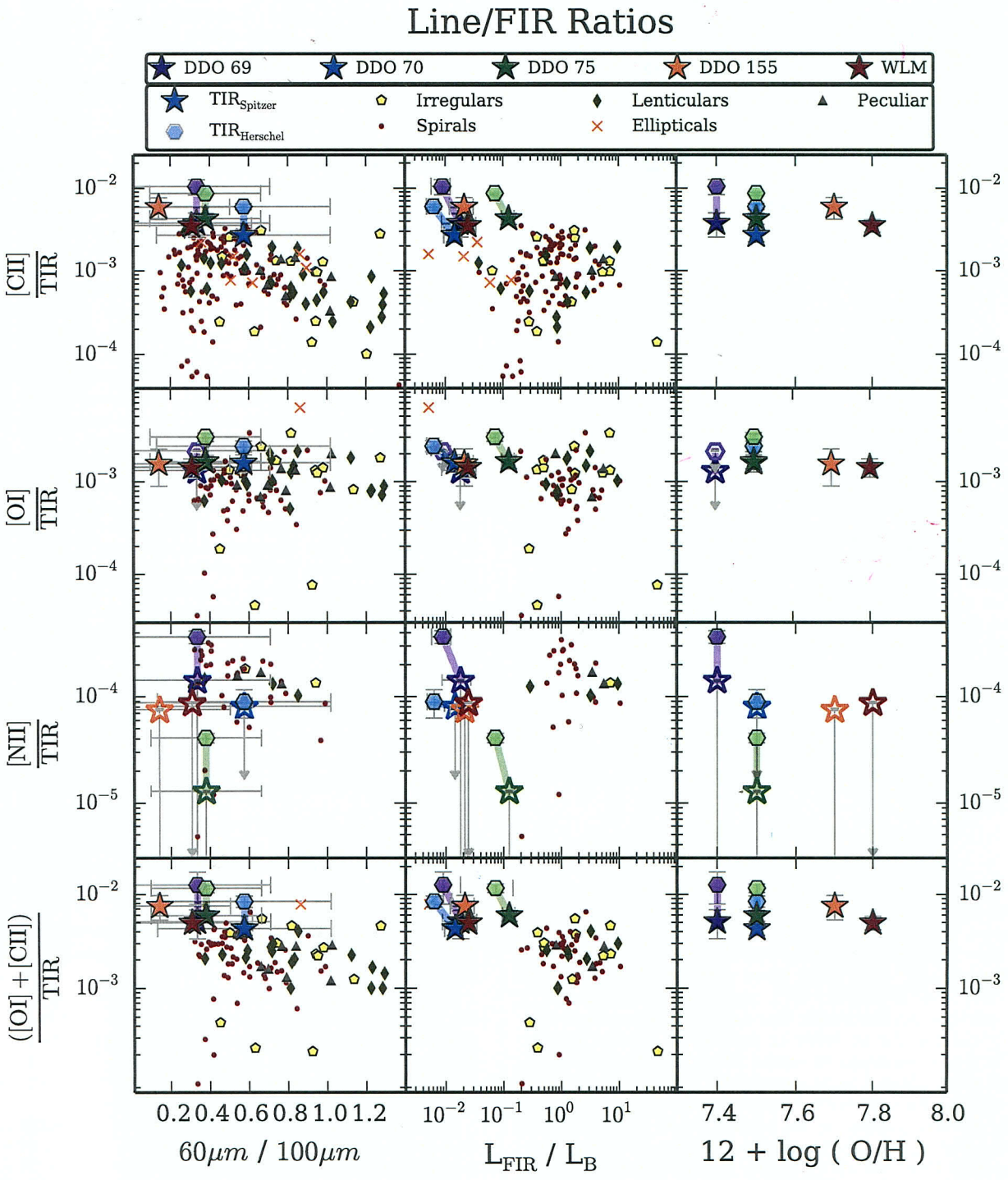

FIG. 8.— PACS and Spitzer TIR line ratios. The spiral, elliptical, and irregular galaxy markers are the same as those described in Figure 7. Again, we only plot those data points from Brauher, et al. (2008) with published detections. The hexagons represent FIR and TIR determined from PACS 100μm, where available, and colored lines linking to the *Spitzer* points (stars) emphasize the differences.

TABLE 5
COMBINED LINE RATIO STATISTICS FOR OUR BULK OBSERVATIONS

Ratio	Mean	Standard Deviation
[O I]/[C II]	0.365	0.115
[O III]/[C II]	0.297	0.212
[O III]/[O I]	1.050	0.655
[O III]/[N II]	38.09	48.36
[N II]/[C II]	0.016	0.013
[C II]/TIR	0.0041	0.0011
[O I]/TIR	0.0016	0.0001
[N II]/TIR	...	...
([O I]+[C II])/TIR	0.0056	0.0011

NOTE. — Mean and standard deviation values of the line ratios of large-scale regions. Only detections are included.

3.8. *Comparison to Multi-Wavelength Data*

There are some qualitative trends apparent in the comparison of maps at different wavelengths of the same regions in each galaxy. To visualize this, we plot our *Herschel* maps side-by-side with H I, V-band, FUV, Hα, and *Spitzer* MIPS 24μm and 160μm images. (See Figure 3 for DDO 155; the other galaxies are available in the online edition.) For DDO 155, the two bright regions that appear in the [C II] map are clearly identifiable in all but the [N II] and 160μm images. It is notable in particular that the [C II] peaks coincide with the FUV, Hα, and 24μm knots, since these are often used as indicators of star formation. Of further interest is the fact that the [C II] peaks are cospatial with regions of high H I density. The [C II]-H I correlation is striking in the rest of our galaxies, as well. DDO 69, in particular, exhibits almost perfect spatial agreement between the two. DDO 70, DDO 75, and WLM show the H I offset ever so slightly from the [C II] peaks. The star formation tracers, as well, are offset but nearby (within $\sim$15″) for every observed region. We discuss the 2D relationship in more detail in our forthcoming paper (Cigan, et al., in preparation).

4. DISCUSSION

4.1. *Large-Scale Trends*

Several past studies have probed the relations of the various FIR lines to FIR colors in dwarfs, such as Malhotra, et al. (2001, hereafter M+01), H+01, and B+08. These previous works were based on spatially unresolved observations. The large beam sizes of *KAO* (FWHM $\sim$55″), *ISO* (FWHM $\sim$75″), and *IRAS* (FWHM $\sim$90″) in previous studies meant that a single measurement usually covered the majority or entirety of a dwarf galaxy. Our single pointings represent small regions (200-500pc per side) within a particular galaxy, and while each footprint can include several large star-forming complexes, we are still probing much smaller scales than the pre-*Herschel* works. Newer studies utilizing *Herschel*, such as DGS (Madden, et al. 2013), KINGFISH (Kennicutt, et al. 2011) and SHINING (e.g., Sturm, et al. 2010), often have a mix of single pointings and mosaicked maps bridging the gap between the small (molecular cloud) and large (star-forming cloud complex) scales. Our sample is the first to probe the FIR line emission of normal dwarfs with low metallicity and moderate star formation rates at these spatial scales.

Figure 7 shows various PACS FIR line ratios – [O I]/[C II], [O III]/[C II], [O III]/[O I], and [N II]/[C II] plotted against typical diagnostics 60μm/100μm and L_{FIR}/L_B. Figure 8 shows ratios of PACS lines to integrated TIR fluxes from *Spitzer* – [C II]/TIR, [N II]/TIR, and ([O I]+[C II])/TIR. We include background data for many giant galaxy types presented by B+08 for comparison. One general trend across many plots is that the various *Herschel* line values in our dwarfs tend to be quite high when compared to *Spitzer* TIR emission. This could potentially indicate that F_{TIR} is generally weak on small scales within our galaxies, or that TIR emission is simply much more spatially extended than that of the FIR fine structure lines, as discussed below.

The FIR color 60μm/100μm, often taken as a proxy for dust temperature or dust heating intensity, is typically quite low in our sample (typically around 0.3), though the errors in the IRAS observations are relatively large. Low 60μm/100μm ratios (low dust temperature) in dwarfs have been discussed in the literature: H+01, in their comparison of [C II]/$f_{15\mu m}$ to 60μm/100μm, interpreted the dust as being cooler than in spirals because it's farther away, on average, from hot stars.

We also note quite low ratios of FIR/B in much of our sample. This could simply result from a reduction in thermal FIR radiation due to lower levels of dust and cool gas. The TIR continuum in our galaxies is low compared to the spectral line emission, but not nearly enough to account for the two orders of magnitude separating our FIR/B values from those in previous studies. High B values could indicate high star formation in our galaxies, but our ancillary suggest otherwise. Alternatively, high B relative to FIR suggests that there is little extinction, or less starlight is processed by dust, which is at least partly a result of the low metallicities – and lower dust content – of these galaxies. The porous nature of the ISM at low metallicities can allow optical light to pass with less attenuation. Our galaxies have much lower metallicity than the B+08 sample, giving credence to this latter explanation.

There are no apparent trends with metallicity among the detected line ratios. There may be some relations between the three ratios including [O III] and metallicity, however the error bars are too large to make any strong claims.

The mean and dispersion for each flux ratio is given in Table 5. We now discuss the results of each set of line ratios in detail.

[O I]/[C II]: When compared to the 60μm/100μm ratio, our galaxies appear to lay in a region more typical of spirals than irregulars. Though both ratios are low in our galaxies, there is a large uncertainty in the 60μm/100μm ratio, which could potentially place the targets studied here back with many of the other irregulars.

We find no strong trend with [O I]/[C II] for increasing dust heating intenstiy as traced by 60μm/100μm within our sample, though there may be a slight increase. M+01 and B+08 noted a much stronger positive correlation, with [O I] dominating the ISM cooling in warmer environments (larger 60μm/100μm ratio). The transition point they find is 60μm/100μm$\approx$0.8. Our sample falls well below this mark, and thus our ratios of less than one ([C II]-dominant) are consistent with the trend. We

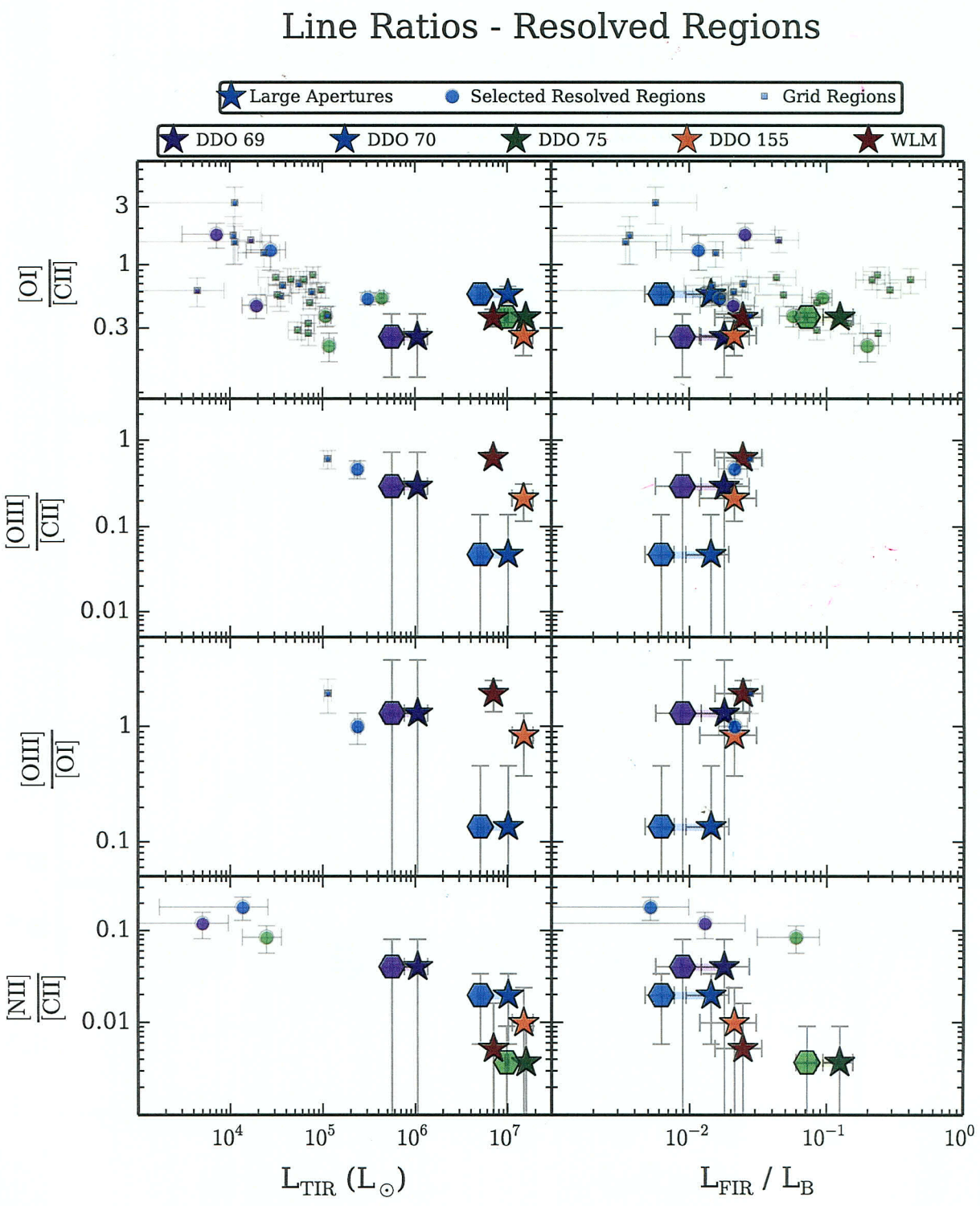

FIG. 9.— *Herschel* line ratio comparison for resolved regions and beam-by-beam grids. These regions are much smaller than the limiting MIPS 160μm beam size for the *Spitzer*-based TIR, so all L_{TIR} values plotted come from the PACS 100μm maps. The one exception is FIR/B value for the [N II] detection in WLM, for which there are no PACS photometry maps. For this single data point, we use the larger-area MIPS FIR/B ratio as an average value for the region.

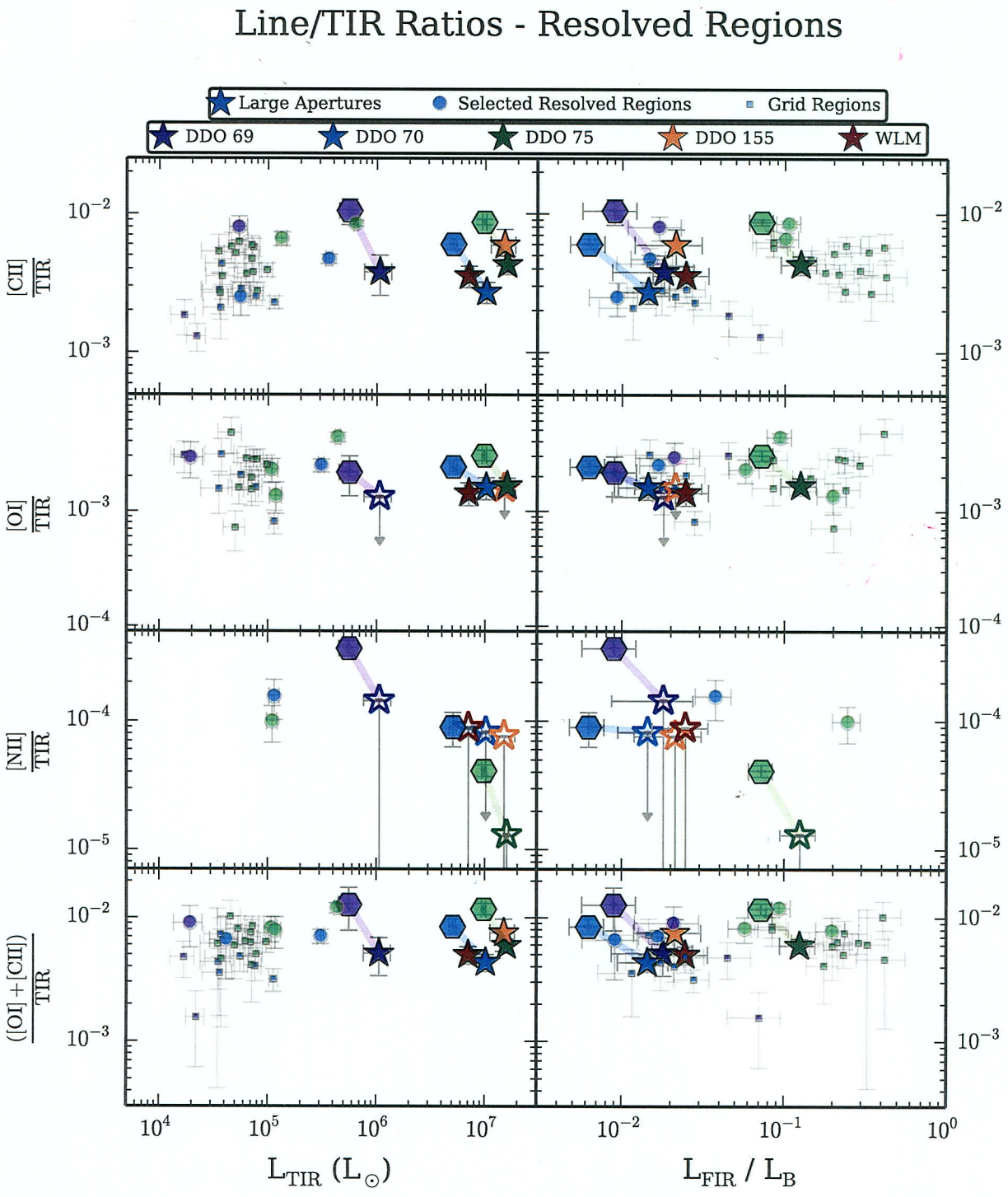

FIG. 10.— *Herschel* line ratio comparison for resolved regions and beam-by-beam grids. Only galaxies with *Herschel* photometry are plotted, so that the TIR beam size matches the small scales.

find no apparent trend within our galaxies for FIR/B, but our dwarfs fall more or less in line with trend from other irregulars and spirals in the B+08 sample.

[O III]/[C II]: One striking result is the fact that we see low [O III] to [C II] ratios (less than unity) compared with other dwarf galaxies. Previous works (H+01; Cormier, et al. 2012; Madden, et al. 2013) have shown typical values of [O III]/[C II] in dwarfs to be in the range of two to five times what we observe. [O III] is often the brightest FIR line observed in starburst galaxies, but our galaxies are much more quiescent star-formers. [O III] is produced by O and B stars in H II regions; the low ratio could indicate a dearth of these large stars near our observed regions, or in the systems in general. This is not simply linked to decreasing metallicity – WLM has the lowest [O III]/[C II] ratio, but also the highest metallicity, in our sample. The comparison with FIR/B shows that our objects really seem to be set apart from previous works. Not only are the FIR/B values lower than for other galaxies, but the [O III]/[C II] ratios are much less than expected for the trend noticed among the other objects.

[O III]/[O I]: The [O III] emission does not vary much with $60\mu m/100\mu m$, extending the similar conclusion for other dIrrs to lower dust temperatures – with the exception of the abnormally low ratio for DDO 70. As noted by H+01, and B+08, irregulars show an elevated [O III]/[O I] ratio compared with spirals, and our observations tend to agree. [O III]/[O I] as compared with FIR/B looks almost identical to the [O III]/[C II] comparison - our galaxies do not follow the noted relation seen in the B+08 sample of irregulars, and indeed appear to be completely separate from the other populations.

[N II]/[C II]: Since [N II] only comes from the diffuse ionized gas (and not PDR gas), the ratio of [N II] to [C II] will increase for environments where a higher fraction of the [C II] emission comes from ionized hydrogen regions. We might expect, therefore, to see a positive trend with heating intensity. However, there is no obvious trend in the [N II]/[C II] ratio with changing $60\mu m/100\mu m$ dust temperature, which is consistent with the findings of M+01 and B+08. Our dwarfs show very low ratios compared to previous studies. DDO 69 has a similar ratio to the lowest in the B+08 sample, but WLM and DDO 75 are an order of magnitude lower. It appears that those in our sample with higher [N II]/[C II] have lower FIR/B – suggesting that as extinction increases, the fraction of diffuse ionized component of [C II] emission decreases. Most of the data points using $\mathrm{FIR}_{Spitzer}$ fall within the error bars of each other, but the data using $\mathrm{FIR}_{Herschel}$ show this trend as well.

[O III]/[N II]: Both species originate in highly ionized regions, however [O III] comes from higher density regions while [N II] comes from lower density regions. The different energies required to create them – 14.5eV for [N II], 35.1eV for [O III] – can also tell us about the harshness of the radiation field. B+08 only hint at possible correlations with $100\mu m/160\mu m$ and FIR/B for their sample, due to insufficient detections. If there are any trends with previous samples, our data do not explicitly verify them. Our own sample lightly suggests the possibility of a decreasing trend with $100\mu m/160\mu m$, and increasing trends with FIR/B and metallicity, though the sizes of the error bars hamper these claims.

[C II]/TIR: Our data follow the slightly decreasing trend of [C II]/TIR with increasing $60\mu m/100\mu m$, seen often in the literature (Malhotra, et al. 1997; Luhman, et al. 1998; Leech, et al. 1999; Negishi, et al. 2001; B+08). With [C II] levels around 0.4% of $\mathrm{TIR}_{Spitzer}$ for most of our sample, and near 1% of the *Herschel*-based TIR, our galaxies reside above most of the B+08 sample – the vast majority of other galaxies of all morphologies have [C II]/TIR ratios of less than 0.4%. Considering that a typical high [C II]-to-*FIR* ratio for irregulars is ≈1% (Madden 2000), and that TIR is often about two times greater than FIR, our galaxies have high ratios indeed, though the highest reported detected [C II]/FIR of 2.2% comes from the N159 region of the Large Magellanic Cloud (Israel, et al. 1996). We find a spread for our five galaxies of $0.25 \pm 0.05\%$ up to $0.59 \pm 0.17\%$ (for $[\mathrm{C\ II}]/\mathrm{TIR}_{Spitzer}$, using $\mathrm{TIR}_{Herschel}$ this becomes 0.54 ± 0.05 to 0.94 ± 0.19).

One possible explanation for the high observed ratios is ~~that it could be~~ a spatial selection effect. Our galaxies are unresolved by the IRAS measurements, meaning that the F_{TIR} calculated from IRAS 60μm and 100μm for the comparison sample is averaged over the whole galaxy. These new data, on the contrary, can resolve features within the galaxies which may have local enhancements of [C II] emission. If we use the IRAS measurements, which are galaxy averages, to calculate TIR instead of the finer-resolution *Spitzer* maps, we find ratios that are more consistent with results published using other IRAS measurements.We do not believe that our numbers are wrong, however – integration of MIPS 70μm flux over regions that cover roughly the entirety of each galaxy gives results that are quite close to the global IRAS 60μm values.

Another possible explanation is based on dust, discussed by Rubin, et al. (2009). FIR emission comes from dust heating by the photoelectric effect. Less dust (often correlated with low metallicity) means that FUV radiation can pass through the ISM without as much attenuation. Thus less dust can mean less FIR emission, which would boost the [C II]/TIR ratio. – Need to talk to Suzanne about this again; some time ago she mentioned that this wasn't true, and I don't remember why...

The high ratio of [C II]to-TIR for $60\mu m/100\mu m$ between 0.3-0.6 is discussed briefly by B+08. They propose that either there is a high fraction of intermediate-mass stars that produce copious amounts of UV and [C II] radiation, or that there is simply a dearth of FIR emission. The low [O III]/[C II] ratios observed in our galaxies are consistent with the latter hypothesis.

Our galaxies tend to have similar FIR/B values to ellipticals. However, the high [C II]/TIR ratios set them apart. This combination implies low dust content in our galaxies. References to dust content vs C/H – Schmidt et al.

[O I]/TIR: Again, we see higher [O I]/TIR ratios than for most other galaxies. There is no strong trend with FIR color or FIR/B, however. M+01 noted that since [O I] emission is more susceptible to absorption by small interstellar particles, the fact that there is no decrease in [O I]/TIR as FIR/B increases could indicate that there is little extinction in the systems we observe.

[N II]/TIR: B+08 found all of their data to be below

at high end of what is observed

[N II]/TIR$\sim$0.001, with some upper limits on the order of 0.006. There were several spiral galaxies listed as detections with ratios down to a few times 10^{-6}. Our galaxies only have upper limits – when [N II] is convolved to the MIPS 160μm beam size – of 0.0001. For those with *Herschel* photometry, the results are scattered: DDO 69 has a relatively high value, and along with DDO 70, these fall in line with the general negative correlation seen in the B+08 sample with $60\mu m/100\mu m$. If we were to consider the non-convolved [N II] detections for DDO 155 and WLM as compared to $\mathrm{TIR}_{Spitzer}$, they would fall near the detected values DDO 70 and DDO 75 using $\mathrm{TIR}_{Herschel}$. The plot in Figure 8 shows the difference between our ratios with FIR/B from previous studies quite dramatically. Our upper limits still mostly agree with the negative correlation between $60\mu m/100\mu m$ reported by M+01, within the large *IRAS* errors, but the *Herschel* photometry knocks them down to a regime shared only by a couple of extreme spirals. The reader is again cautioned that the [N II] fluxes are not overly reliable when compared to the much coarser *Spitzer* data, since they come from small disparate regions in the maps only noticed upon careful inspection.

([O I]+[C II])/TIR:

The ratio of ([O I]+[C II]) to TIR is a diagnostic of gas heating efficiency of PDRs in galaxies, as discussed by Hollenback & Tielens (1997). In short, TIR emission traces the gas heating, while [C II] and [O I] trace the gas cooling. Assuming that the photoelectric effect on dust is responsible for the gas heating, the ratio of ([O I]+[C II])/TIR is thus a proxy for the photoelectric efficiency.

We note that since [C II] is dominant over [O I], the trend looks almost the same as that in the [C II]/TIR comparison. The background galaxy sample from B+08, also similar to that in [C II]/TIR, has significant scatter for irregulars and spirals on the lower half of the plot. M+01 showed a decreasing trend for this ratio with respect to increasing $60\mu m/100\mu m$, and our data fall nicely in line with this trend, indicating that our sample consists of efficient coolers. There is no obvious trend with FIR/B within our galaxies, though ignoring the low-end scatter in the B+08 sample, there may be a slight downward trend overall.

4.2. *Spatially-Resolved Trends*

The various FIR line ratios in discrete resolved regions within our galaxies are compared to FIR/B as well as integrated TIR luminosity in Figures 9 and 10. As discussed in § 3.3, the targeted resolved regions for a given line ratio were selected based on the locations of the limiting line signal, while the gridded regions were objectively defined by dividing the maps into uniform chunks the size of the [C II] beam. The MIPS 160μm data, which go into the calculation of TIR luminosity, have a PSF that is nearly the size of each *Herschel* footprint, meaning several of the individually resolved and gridded regions would be contained within one *Spitzer* TIR beam. For this reason, only *Herschel*-based TIR values are considered for these smaller regions.

All resolved line-line ratios exhibit negative trends with increasing L_{TIR}, though there are admittedly few detections on these scales aside from those of the [C II] line – of the galaxies with *Herschel* photometry, only DDO 70 has reliable resolved [O III] detections, meaning that the individual regions have S/N$\geq$3. The [O I]/[C II] values for the whole-image integrations (sum of targeted [O I] regions – the large stars in the plots) remain roughly constant between roughly 0.3 and 0.5, however there are distinct inverse trends with TIR across the differently-sized regions. Though the other line ratios have fewer data points, they also exhibit negative relations with TIR.

The result of these negative trends is that as TIR increases, [C II] becomes more dominant over [O I], [O III], and [N II], while [O I] becomes more dominant over [O III]. [C II] dominating [O I] is an indication of cooler environments. As [O III] and [N II] decrease relative to [C II] with increasing TIR, less of the observed emission is coming from hot ionized regions, which suggests we are probing more and more into PDRs in those cases. Decreasing [O III] relative to [O I] also supports this idea, as it indicates that more emission comes from the neutral phase as TIR increases. As [O I]/[C II] is an indicator of environment temperature and [N II]/[C II] denotes the diffuse (warm) vs. PDR (cool) component of singly-ionized carbon, a decrease in [O I]/[C II] and [N II]/[C II] with increasing TIR luminosity could also simply be evidence that hotter regions are inhospitable to dust. The hotter environments have less TIR emission, suggesting that the dust there has been destroyed. These trends are mild between the large apertures representing the "total" emission in each of our galaxies, but this also appears to be true for the smaller resolved regions.

The [O III]/[C II] and [O III]/[O I] ratios detected in DDO 70 show positive trends with FIR/B. The increases with FIR/B are not enough to shift these regions into the realm of the starburst dwarfs, however. Since TIR decreases as both ratios increase, B-band emission must necessarily decrease more rapidly than TIR within these regions to avoid the paradoxical interpretation that extinction goes up as dust content goes down. These plots then suggest that as dust content and B go down, the ionized oxygen fraction increases slightly, though the ratios are still below about unity.

[N II]/[C II] has no apparent relation with FIR/B between the different scales for any of our galaxies. [O I]/[C II] appears to share this fate as well, though DDO 69 may have a slightly increasing trend with region size as FIR/B increases.

5. SUMMARY

We have presented *Herschel* PACS spectroscopy of a sample of five dwarf galaxies from the Little Things Survey – DDO 69, DDO 70, DDO 75, DDO 155, and WLM. All five galaxies are faint, low-metallicity, nearby dwarfs with moderate star formation. Prior to *Herschel*, these types of systems were extremely difficult to observe in the FIR, but these recent detections now make it possible to explore the regime of normal dwarfs, not undergoing starburst episodes, on the scales of large star-forming complexes.

We observed four fine structure lines in each galaxy: [C II]158μm, [O I]63μm, [O III]88μm, and [N II]122μm, with the exception of DDO 75 which had no [O III] observations. [C II] and [O I] are important species in the PDR cooling process, while [O III] and [N II] are indicators of regions with ionized gas. We compare to the total

infrared continuum as estimated by a *Spitzer* 24, 70, and 160μm maps, though the coarse resolution of the MIPS maps effectively limits $TIR_{Spitzer}$ to average values over most of the majority of the PACS maps. Where available, we also utilize new PACS 100μm observations to estimate TIR at the same resolution as the line emission.

The dwarfs in our sample have low FIR/B as well as low $60\mu m/100\mu m$, indicating cooler dust on average than other dIrrs and spirals. Thus they are at one extreme, having low temperature, low dust content, and low metallicity (5-13% of $Z_{\odot}$).

Upon examination of several line ratios and comparisons with previous studies of other galaxies, we find:

- The [C II]/TIR ratios in all of our galaxies are very high, on the order of 0.2-1%, and are nearly two times that of starburst dIrrs. There is no appreciable trend within our sample for increasing $60\mu m/100\mu m$ or FIR/B emission, though our data are consistent with previously noted negative trend with increasing dust temperature when we consider all galaxy types.

- [O I]/TIR values are also quite high, which is consistent with the picture of low extinction in our systems.

- High ([O I]+[C II])/TIR, where [O I] and [C II] are primary coolants and TIR comes from primary heating processes, suggests high cooling efficiency at low dust temperature.

- Our galaxies have low observed [O I]/[C II] ratios – smaller than most other dIrrs, but still following the trend with $60\mu m/100\mu m$ across all galaxy types seen by Brauher, et al. (2008). The low line ratio values are an indication of cooler environments, which is consistent with the relatively low dust temperatures implied by the FIR color.

- The [O III]/[C II] ratios are in general lower in our sample than for dwarfs with high star formation rates, but are roughly similar to spirals. This is due in part to the fact that we observe galaxies that are undergoing moderate star formation, and as such should have fewer hot ionized regions traced by [O III]. The data from resolved regions in DDO 70 suggest that B-band emission decreases faster than TIR.

- [N II] emission, which comes from ionized gas, is generally not widely detected in our observations, implying that the [C II] emission is primarily coming from PDRs rather than H II regions. Though previous studies have shown a generally positive trend between [N II]/[C II] and FIR/B, we see a slight decrease in [N II]/[C II] for increasing FIR/B among our galaxies using large integration apertures.

Acknowledgments: Funding for this project was provided by NASA JPL RSA grant 1433776. The National Radio Astronomy Observatory is a facility of the National Science Foundation operated under cooperative agreement by Associated Universities, Inc.

Facilities: *Herschel* (PACS), Very Large Array

REFERENCES

Aniano, G., Draine, B. T., Gordon, K. D., & Sandstrom, K. 2011, PASP, 123, 1218
Asplund, M., et al. 2009, ARA&A, 47, 481
Bolatto, A. D., Jackson, J. M., & Ingalls, J. G., ApJ, 513, 275
Bolatto, A. D., Leroy, A. K., Rosolowsky, E., et al. 2008, ApJ, 686, 948
Bot, C., Boulanger, F., Rubio, M., & Rantakyro, F. 2007, A&A, 471, 103
Brauher, J. R., Dale, D. A.,& Helou, G. 2008, ApJS, 178, 280
Burstein, D., & Heiles, C. 1984, ApJS, 54, 33
Cormier, D., et al. 2012, A& A, 548A, 20
Dale, D. A., Helou, G., Contursi, A., Silbermann, N. A. Kolhatkar, S. 2001 ApJ, 549, 215
Dale, D. A., & Helou, G. 2002, ApJ, 576, 159
Dale, D. A., et al. 2009, ApJ, 703, 517
Dolphin, A. E., Saha, A., Claver, J., et al. 2002, AJ, 123, 3154
Dolphin, A. E., Saha, A., Skillman, E. D., et al. 2003, AJ, 125, 1261
Draine, B. T., & Li, A. 2007, ApJ, 657, 810
Engelbracht C. W. et al., 2007, PASP, 119, 994
Fruchter, A. S., & Hook, R. N. 2002, PASP, 114, 144
Galametz, M., Kennicutt, R. C., et al., 2013, MNRAS, 431, 1956
Gieren, W., Pietrzyński, G., Szewczyk, O., et al. 2008, ApJ, 683, 611
Gordon K. D. et al., 2007, PASP, 119, 1019
Heiles, C. 1994, ApJ, 436, 720
Helou, G., Khan, I. R., Malek, L., & Boehmer, L. 1988, ApJS, 68, 151
Hollenbach, D. J., & Tielens, A. G. G. M. 1997, ARA& A, 35, 179
Hunt, L. K., Thuan, T. X., Izotov, Y. I., & Sauvage, M., 2010, ApJ, 712, 164
Hunter, D. A., Gallagher, J. S., Rice, W. L., & Gillett, F. C. 1989, ApJ, 336, 152
Hunter, D. A., Kaufman, M., et al. 2001, ApJ, 553, 121
Hunter, D. A., & Elmegreen, B. G. 2004, AJ, 128, 2170
Hunter, D. A., & Elmegreen, B. G. 2006, ApJS, 162, 49
Hunter, D. A., Elmegreen, B. G., & Ludka, B. C. 2010, AJ, 139, 447
Hunter, D. A., Ficut-Vicas, D., Ashley, T., et al. 2012, AJ, 144, 134
Israel, F. P., Maloney, P. R., Geis, N., et al. 1996, ApJ, 465, 738
Kaufman, M. J., Wolfire, M. G., Hollenbach, D. J., & Luhman, M. L., ApJ, 527, 795
Kaufman, M. J., Wolfire, M. G., & Hollenbach, D. J. 2006, ApJ, 644, 283
Kennicutt, R. C., et al. 2011, PASP, 123, 1347
Kniazev, A. Y., Grebel, E. K., Pustilnik, S. A., Pramskij, A. G., & Zucker, D. B. 2005, AJ, 130, 1558
Lebouteiller, V., et al., 2012, A&A, 548, A91
Lee, H., Skillman, E. D., & Venn, K. A. 2005, ApJ, 620, 223
Leech, K. J., et al., 1999, MNRAS, 310, 317
Leroy, A. K., Bolatto, A. D., Stanimirovic, S., et al., 2007, ApJ, 658, 1027
Leroy, A. K., et al., 2008, AJ, 136, 2782
Leroy, A. K., Walter, F., Bigiel, F., et al. 2009, 137, 4670
Lisenfeld, U., et al. 2007, A&A, 462, 507
Luhman, M. L., et al., 1998, ApJ, 504, L11
Madden S. C., Geis N., Genzel R., Herrmann F., Jackson J., Poglitsch A., Stacey G. J., Townes C. H., 1993, ApJ, 407, 579
Madden, S. C., Poglitsch, A., Geis, N., Stacey, G. J., & Townes, C. H., 1997, ApJ, 483, 200
Madden, S. C. 2000, New A Rev., 44, 249
Madden, S. C., et al., 2013, PASP, 125, 600
Malhotra, S., et al. 1997, ApJ, 491, L27
Malhotra, S., et al. 2001, ApJ, 561, 766
Maloney, P. & Black, J. H., 1988, ApJ, 325, 389

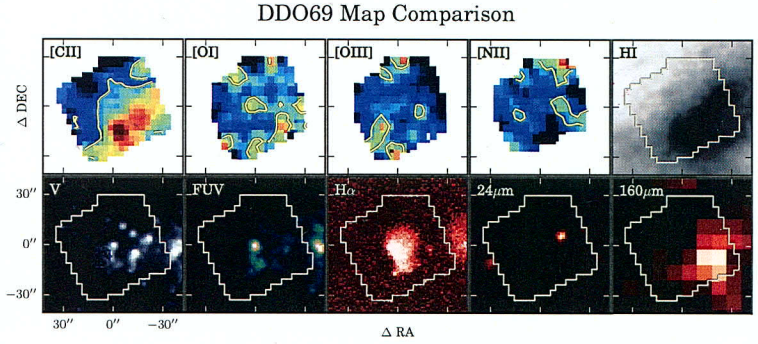

(a) (b)

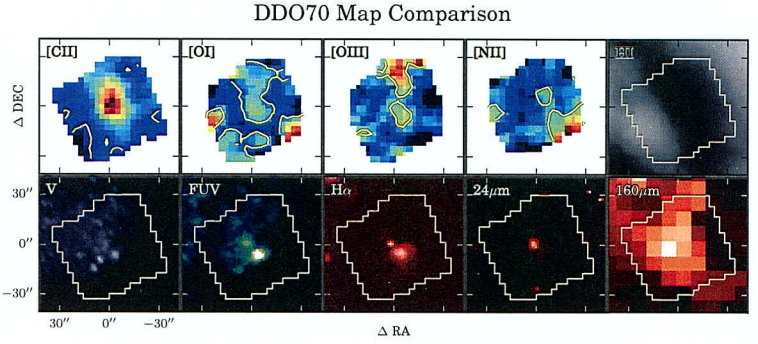

(c)

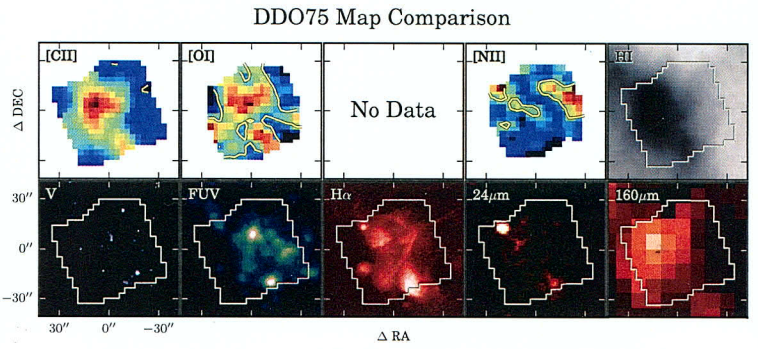

(d)

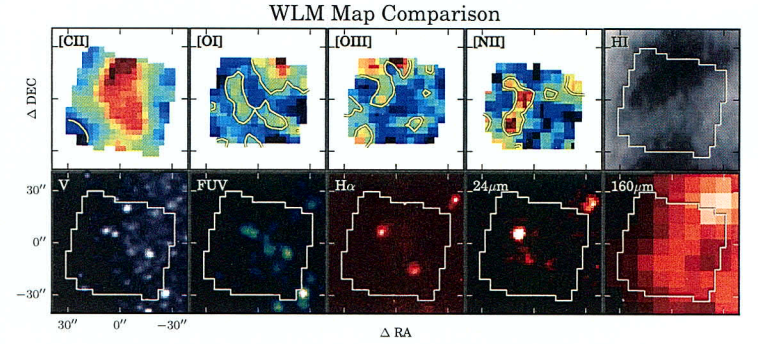

FIG. 12.— *Online-only figures.* Comparison of emission in the *Herschel* maps with other observations at several wavelengths. For all four galaxies: H I is from Hunter, et al. (2012), V from Hunter & Elmegreen (2006), FUV from Hunter, et al. (2006), Hα from Hunter & Elmegreen (2004), 24μm & 160μm from Dale, et al. (2009). We note that, in general, [C II] emission correlates well with H I emission, and bright knots in the bands that trace star formation are often near [C II] peaks. The occasional smudges in the V-band images are artifacts from removing foreground stars and background galaxies.

I don't think they are visible this way the images are displayed. You have to see the noise in the background for that.